Available online at www.sciencedirect.com
ScienceDirect
Geochimica et Cosmochimica Acta 71 (2007) 984–1008
Geochimica
www.elsevier.com/locate/gca

Chemical and structural control of the partitioning of Co, Ce, and Pb in marine ferromanganese oxides

Yoshio Takahashi [a,b,*], Alain Manceau [c], Nicolas Geoffroy [c], Matthew A. Marcus [d], Akira Usui [e]

[a] Department of Earth and Planetary Systems Science, Graduate School of Science, Hiroshima University, Higashi-Hiroshima, Hiroshima 739-8526, Japan
[b] Laboratory for Multiple Isotope Research for Astro- and Geochemical Evolution (MIRAGE), Hiroshima University, Hiroshima 739-8526, Japan
[c] Environmental Geochemistry Group, LGIT, University J. Fourier and CNRS, BP 53, 38041 Grenoble Cedex 9, France
[d] Advanced Light Source, Lawrence Berkeley National Laboratory, One Cyclotron Road, Berkeley, CA 94720, USA
[e] Department of Natural Environmental Science, Faculty of Science, Kochi University, Kochi-shi, Kochi 780-8520, Japan

Received 21 July 2006; accepted in revised form 1 November 2006

Abstract

The oxidation state and mineral phase association of Co, Ce, and Pb in hydrogenetic, diagenetic, and hydrothermal marine ferromanganese oxides were characterized by X-ray absorption near-edge structure (XANES) and extended X-ray absorption fine structure (EXAFS) spectroscopy and chemical extraction. Cobalt is trivalent and associated exclusively with the Mn oxide component (vernadite). Cerium is tetravalent in all genetic-type oxides (detection limit for Ce(III) $\sim$ 5 at. %), including Fe-rich areas (ferrihydrite) of hydrogenetic oxides, and is associated primarily with vernadite. Thus, the extent of a Ce anomaly does not result from variations in redox conditions, but appears to be kinetically controlled, decreasing when the growth rate increases from hydrogenetic to diagenetic to hydrothermal oxides. Lead is divalent and associated with Mn and Fe oxides in variable proportions. According to EXAFS data, Pb is mostly sorbed on edge sites at chain terminations in Fe oxide and at layer edges in Mn oxide (ES complex), and also on interlayer vacancy sites in Mn oxide (TCS complex). Sequential leaching experiments, spectroscopic data, and electrochemical considerations suggest that the geochemical partitioning in favor of the Mn oxide component decreases from Co to Ce to Pb, and depends on their oxidative scavenging by Mn and Fe oxides.

1. Introduction

Marine ferromanganese oxides are found in a variety of environments and forms, such as hydrogenetic nodules and crusts on the deep-sea floor, diagenetic precipitates in sediments, hydrothermal deposits near oceanic ridges, and sinking Fe–Mn colloidal particles in the water column (Glasby, 2000). A common trait to all ferromanganese oxides is their enrichment in trace elements relative to seawater. Their ubiquity, abundance, and importance in the cycling of trace elements has aroused the interest of scientists for several decades, in particular with respect to the geochemical partitioning and incorporation mechanisms of trace elements. These questions often have been addressed by interelement correlations using bulk chemical analysis (e.g., Moorby and Cronan, 1981; Calvert and Piper, 1984; Aplin and Cronan, 1985a,b; De Carlo and McMurtry, 1992; Wen et al., 1997), and selective dissolution (Moorby and Cronan, 1981; Aplin and Cronan, 1985b; Koschinsky and Halbach, 1995; Koschinsky and Hein, 2003). Few studies have used non-invasive spectroscopic methods, although they offer direct, and often unique, access to the problem (e.g., Dillard et al., 1982; Takahashi et al., 2000; Kuhn et al., 2003; Marcus et al., 2004a).

In this paper, the oxidation states of Co, Ce, and Pb in hydrogenetic, diagenetic, and hydrothermal ferromanganese oxides were determined by X-ray absorption near-edge

* Corresponding author. Fax: +81 82 424 0735.
E-mail address: ytakaha@hiroshima-u.ac.jp (Y. Takahashi).

0016-7037/$ - see front matter © 2006 Elsevier Inc. All rights reserved.
doi:10.1016/j.gca.2006.11.016

structure (XANES) spectroscopy to evaluate the importance of redox reactions in trace element partitioning (Goldberg, 1961, 1965; Goldberg et al., 1963; Piper, 1974; Burns, 1976). Dillard et al. (1982) concluded using X-ray photoelectron spectroscopy (XPS) that cobalt is trivalent in marine ferromanganese oxides, and Takahashi et al. (2000) that cerium is tetravalent using XANES spectroscopy. These two studies were limited to metal-rich hydrogenetic samples. Pb enrichment in ferromanganese oxides has been suggested to result from Pb(II) to Pb(IV) oxidation (Goldberg, 1965; Murray and Dillard, 1979), but this hypothesis has received little experimental support (Dillard et al., 1981). The abundances of Co, Ce, and Pb decrease on average from hydrogenetic to diagenetic to hydrothermal deposits (Usui et al., 1997), and the possibility that this evolution is associated with a variation of their oxidation state has not been investigated. Such a relationship would provide insight into chemical processes responsible for the enrichment of redox-sensitive trace elements in ferromanganese oxides. In particular, questions remain as to the reasons for the variability of the Ce anomaly in REE (rare earth elements) patterns, and its possible link to Ce oxidation state.

When considering redox reactions in ferromanganese oxides, elemental distribution among Mn and Fe oxides is an important issue. The nature of the trace element host phases were investigated by electron microprobe, micro-XANES spectroscopy (μ-XANES), and Pb L_{III}-edge extended X-ray absorption fine structure (EXAFS) spectroscopy, and the results compared to those from sequential leaching to assess the usefulness of chemical extraction to speciate trace metals in ferromanganese matrices.

2. Materials and methods

2.1. Samples

Seventeen samples collected during several research cruises in the Central to NW Pacific Ocean and the Central Indian Ocean were selected for this study (Table 1). They were classified into hydrogenetic (HG), diagenetic (DG), and hydrothermal (HT) origins on the basis of the mineralogy of the Mn oxide, as summarized in Table 1 (Takematsu, 1998). Samples 31GTV2-3 and 31GTV6-11 have a mixed hydrogenetic and hydrothermal origin (Kuhn et al., 1998). The two samples had fast growth rates (10–20 mm/Myr) due to the supply of Mn and Fe from hydrothermal plumes, but their trace elements are considered to be derived mainly from seawater. Thus, they are labeled HT + HG in Table 1. Nodule D465 has a hydrogenetic core and a diagenetic rim and the two parts were analyzed separately. Samples containing P-rich layers were disregarded because secondary phosphatization may modify the original distribution of trace elements (Koschinsky et al., 1997). According to this reference, P concentration in phosphatized crusts is higher than 2.5 wt%, a value well above the P content of our samples (see Section 3).

2.2. Reference materials

CoO (purity > 99.9%), orthorhombic PbO (>99.9%), Pb_3O_4 (>99%), PbO_2 (>99.9%), $CeCl_3$ (>99%), $Ce(SO_4)_2$ (>99.5%), and CeO_2 (>99.9%) from Wako Pure Chemical Industries, Ltd., Katayama Chemicals, and Rare Metallic Co., Ltd. were used as references for XANES measurements. Powders were diluted to 0.5 wt% in boron nitride and pressed into pellets. A $Ce(OH)_4$ gel was prepared by hydrolyzing a $Ce(NH_4)_2(NO_3)_6$ solution at pH 7 in contact with air (Sumaoka et al., 2000). No Ce(IV) reduction occurs at this Eh–pH condition (Brookins, 1988). The $Ce(OH)_4$ gel recovered by filtration was re-suspended in water at pH 7 and adjusted to a 0.5 wt% Ce concentration for XANES analysis.

Ferrihydrite (HFO) and δ-MnO_2 used in Co, Ce, and Pb sorption experiments for XANES measurements were synthesized according to Schwertmann and Cornell (2000) and Murray (1974), respectively. Sorption samples were prepared by adding 10 mL of 17.0 μM Co(II), 7.15 μM Ce(III), or 4.83 μM Pb(II) solutions (pH 5) prepared from nitrate salts to 1 mg ferrihydrite or δ-MnO_2 in suspension in synthetic seawater (Nishimura, 1983) at equilibrium with air. Final pH was adjusted to 7.0 (Co), 6.6 (Ce), and 6.5 (Pb) by incremental addition of HCl. The final pH was lower than that of seawater (8.2 ± 0.1) to prevent metal precipitation. The solid phases were recovered by filtration (0.45 μm; hydrophilic PTFE) after 1 h of reaction time, washed with bidistilled water (Milli-Q), and packed wet into polyethylene bags for XANES measurements. A Ce-sorbed ferrihydrite sample was equilibrated for 120 h. The Ce, Co, and Pb concentrations in the solid phases are about 0.1 wt%.

A separate series of Pb-sorbed δ-MnO_2 samples were prepared as follows for EXAFS measurements. δ-MnO_2 was prepared by reducing at pH 7 a $KMnO_4$ solution with $MnCl_2$ (Villalobos et al., 2005). The precipitate was washed, dialyzed, and stored at 5 °C in polypropylene containers for several days at the synthesized solid concentration (21.7 g/L). Pb-sorption samples were prepared by addition of a $Pb(NO_3)_2$ solution to a δ-MnO_2 suspension (2 g/L, 0.1 M $NaNO_3$) that had been pre-equilibrated at the desired pH with an automatic titrator. After allowing several hours for equilibration at constant pH, the sorption sample was filtered on a 0.1 μm cellulose nitrate membrane, washed with Milli-Q water to prevent the precipitation of metal salt, and freeze-dried. We know from previous studies, and from the similarity of our Pb-EXAFS data (see Section 3) with those collected on wet pastes (Villalobos et al., 2005) and powders frozen to 10–20 K (Morin et al., 2001), that the binding mechanism of hydrolyzable cations on phyllomanganates is not modified by freeze-drying, probably because they form multidentate inner-sphere complexes (Lanson et al., 2002a; Manceau et al., 2002a). Also, the stability in vacuum of the layer of water in the interlayer of δ-MnO_2 and birnessite, which is attested by the persistence of the basal X-ray reflection at ~7 Å, supports the view that data collected on freeze-dried

Table 1
List of the samples of ferromanganese oxides studied in this work

Sample name	Sampling site			Cruise name	Type of deposition	Mineralogy of Mn oxides[a]
	Latitude	Longitude	Depth (m)			
D535	13°00.6′S	159°17.6′W	5222	Hakurei-maru GH83-3	HG	Fe-vernadite
CD25	16°26.0′N	169°32.3′W	2320	Farnella FN-86-HW	HG	Fe-vernadite
AD14	14°11.8′N	167°24.4′E	1617	Hakurei-maru 96S	HG	Fe-vernadite
D1-X1	32°04.5′N	138°31.5′E	2600	Moana Wave MW9503	HG	Fe-vernadite
D21-m3	31°23.5′N	138°45.3′E	1110	Moana Wave MW9503	HG	Fe-vernadite
D465, inner	09°03.4′N	174°04.1′W	5968	Hakurei-maru GH80-5	HG	Fe-vernadite
D465, outer	09°03.4′N	174°04.1′W	5968	Hakurei-maru GH80-5	DG	10 Å-vernadite
D513	01°05.2′S	166°10.0′W	5341	Hakurei-maru GH82-4	DG	10 Å-vernadite
D514	00°45.9′S	166°07.0′W	5200	Hakurei-maru GH82-4	DG	10 Å-vernadite
FG352	03°15.8′N	169°41.1′W	5370	Hakurei-maru GH81-4	DG	10 Å-vernadite
G181	07°01.4′N	171°59.7′W	5660	Hakurei-maru GH76-1	DG	10 Å-vernadite
B6	30°17.8′N	172°10.5′W	5350	Hakurei-maru GH80-1	DG	10 Å-vernadite
F243-1	07°40.2′N	172°56.3′W	5907	Hakurei-maru GH80-1	DG	10 Å-vernadite
D11-X9	32°00.1′N	139°10.1′E	1575	Moana Wave MW9503	HT	10 + 7 Å-vernadite + todorokite
D12-X2	31°58.0′N	139°04.2′E	1590	Moana Wave MW9503	HT	Hexagonal birnessite
D21-103	31°23.5′N	138°45.3′E	1110	Moana Wave MW9503	HT	10 + 7 Å-vernadite + todorokite
31GTV2-3	25°24.0′S	69°45.4′E	2800	SO92 Sonne	HG + HT	Fe-vernadite
31GTV6-11	25°24.0′S	69°45.4′E	2800	SO92 Sonne	HG + HT	Fe-vernadite

[a] Turbostratic (i.e., *c*-disordered) phyllomanganates found in marine ferromanganese oxides have been named δ-MnO_2, buserite and birnessite in the literature on the basis of the intensity and position of basal reflections by XRD. Today, it appears that there is no fundamental structural difference between all these phyllomanganate varieties. As discussed in Manceau et al. (2006), the use of the generic term vernadite, which dates back to long before the three others (Betekhtin, 1940), is preferred to describe natural turbostratic phyllomanganates. In sample D12-X2, the phyllomanganate layers are stacked regularly with a hexagonal sequence as in synthetic HBi (Silvester et al., 1997). Diffraction patterns are presented in Electronic Annex.

samples are representative of surface complexes at the water-mineral interface. Four samples were prepared at pH 5 and Pb/Mn molar ratios, as measured by inductively coupled plasma-atomic emission spectrometry (ICP-AES), of 0.002 (PbdBi2), 0.044 (PbdBi44), 0.112 (PbdBi112), and 0.197 (PbdBi197). One sample was prepared at pH 7 and intermediate surface loading to test the influence of pH on the structure of the Pb surface complex on δ-MnO_2. Its EXAFS spectrum was almost identical to the PbdBi44 spectrum (data not shown). The effect of crystallinity was investigated by comparing the data with those for Pb sorbed on well-crystalline hexagonal birnessite at pH 4 and Pb/Mn molar ratio of 0.031 (sample PbBi31 in Lanson et al., 2002a). This reference had been characterized by EXAFS spectroscopy previously (Manceau et al., 2002a), but a higher quality spectrum was recorded for this study.

2.3. Chemical compositions

The Mn, Fe, Co, Ni, Cu, and Zn concentrations in the natural samples were measured by ICP-AES (Yanaco UOP-1S) after acid digestion using HF/HCl/HNO_3, and Pb concentration was measured by inductively coupled plasma-mass spectrometry (ICP-MS) (VG PQ-3) using Bi as an internal standard. The precision and accuracy of the analytical values were better than 10%, based on the analysis of the JMn-1 reference prepared from ferromanganese oxide deposits distributed by the Geological Survey of Japan (GSJ; Terashima et al., 1995). REE abundances were measured by ICP-MS using In and Bi as internal standards (Takahashi et al., 2000). Repeated analyses on JB-1a standard rock prepared by GSJ showed that the precision and accuracy of the REE analyses were generally better than 5%. REE abundances for D513 are from Ohta et al. (1999), and major and minor (including REE) element concentrations for 31GTV2-3 and 31GTV6-11 are from Kuhn et al. (1998). Major elements and Co, Ni, Cu, Zn, Ce, and Pb concentrations in samples CD25, D535, AD14, D465, D514, and FG352 were measured also with an electron probe microanalyzer (EPMA, JXA-8200, JEOL), running at 15 keV acceleration voltage and using a 5 μm-sized beam.

2.4. Sequential leaching experiments

Sequential leaching experiments were performed on powdered samples, following the procedure described in Koschinsky and Hein (2003) and Koschinsky and Halbach (1995). Briefly, 0.5 g of powder was mixed with 15 mL of 1 M acetic acid/Na acetate buffer (pH 5) at room temperature for 5 h. The filtrate (fraction 1) was considered to include exchangeable cations and cations initially present in carbonates. The residue was suspended in 25 mL of Milli-Q water and stirred with 87.5 mL of a 0.1 M hydroxylamine hydrochloride (NH_3OHCl) solution (pH 2) for 24 h. The filtrate at this step (fraction 2) contained cations originally in Mn oxides. The new residue was suspended in 100 mL of Milli-Q water and stirred with 87.5 mL of 0.2 M oxalic acid/ammonium oxalate buffer (pH 3.5) for 12 h. The filtrate (fraction 3) contained cations originally associated with Fe oxides. The final residue, mainly consisting of silicates and aluminosilicates (fraction 4), was digested for bulk chemical analyses. The Mn, Co, Pb, and Ce concen-

trations in all filtrates were measured by ICP-MS after dilution by a factor >100 in 2% HNO_3, and the Fe concentrations were measured by ICP-AES. For each element, the sum of concentrations from fractions 1 to 4 divided by the bulk concentrations (i.e., recovery of the leaching experiments) was better than 82%.

Re-adsorption of dissolved ions on residual solid phases may occur during sequential leaching experiments (Rendell et al., 1980; Sholkovitz, 1989; Gilmore et al., 2001). The fractions of metals re-adsorbed on Fe oxides and insoluble phases (silicate and aluminosilicates) in the hydroxylamine hydrochloride extraction step were determined using ^{54}Mn, ^{58}Co, ^{139}Ce, and ^{146}Gd radioisotope tracers (Ambe et al., 1995; Takahashi et al., 1997, 1999). Lead radioisotopes were not included in the multitracer solution, and thus Pb was not analyzed. The amounts of re-adsorbed radioisotopes were obtained by measuring the γ-ray spectrum of the filtrate with a Ge solid-state detector. Counting was stopped when the total number of counts was at least 10,000 for each radioisotope. Measurements of the peak area and corrections of the decay of each isotope were carried out by a routine procedure.

2.5. XANES and EXAFS measurements and analyses

Cerium L_{III}-edge and Co K-edge XANES spectra were recorded on beamline BL12C at the KEK Photon Factory in Tsukuba, Japan (Nomura and Koyama, 1996), and Pb-L_{III}-edge XANES spectra on beamline BL01B1 at SPring-8 in Hyogo, Japan (Uruga et al., 1999). The two beamlines have similar layouts. The X-rays were monochromatized with a pair of Si(111) crystals. The beam size at the sample position was about 1×1 mm^2, and its intensity (I_0) monitored with an ionization chamber. The sample was placed at 45° from the incident beam, and the fluorescent X-rays measured with a 19 element Ge solid-state detector. At the Co K-edge, the intensity of the unwanted fluorescence signal from Mn and Fe was reduced by mounting a vanadium filter ($\mu t = 3$ or 6) in front of the detector. Deadtime correction was done by the method of Nomura (1998). Energy was calibrated by assigning the energy of the first peak of CeO_2 at 5730.5 eV (Ce L_{III}-edge), the absorption maximum of CoO (Co K-edge) at 7730.3 eV, and the absorption maximum of PbO_2 (Pb L_{III}-edge) at 13061.5 eV (the first maximum of the derivative of elemental Pb was at 13029 eV). XANES spectra were recorded with a 0.25–1 eV step size and 1–5 s counting per step. One to five scans were summed to improve the signal-to-noise ratio, and all spectra were normalized to unit step in the absorption coefficient. No radiation damage was detected during the data acquisition.

Bulk XANES measurements were complemented by micro-XANES and X-ray fluorescence (XRF) mapping measurements for the hydrogenetic ferromanganese nodule CD25. The experiments were carried out on beamline 10.3.2 at the Advanced Light Source (ALS), Lawrence Berkeley National Laboratory, USA (Manceau et al., 2002b; Marcus et al., 2004b). The sample was embedded in a high purity resin (Eposet, Maruto Co., Ltd.), polished on one face, and glued on a glass slide with a wax product (Skywax 415, Maruto Co., Ltd.). After polishing the other face of the sample to a thickness of about 30 μm, the thin section was removed from the glass support by dissolving the wax in *o*-xylene. An area of 1.2×1.1 mm^2 from the free-standing specimen was scanned under a 5×5 μm^2 beam using steps of 5 μm. The distribution of Co and Ce were imaged by recording, for each element, one map above and another below their absorption K edges (7659 and 7759 eV for Co; 5718 and 5730.5 eV for Ce, respectively) and calculating the difference maps. From visual comparison of these elemental distributions, and from the Mn/Fe ratio, specific points-of-interest (POIs) were selected for Co K-edge and Ce L_{III}-edge micro XANES measurements. To avoid the possibility of radiation damage, only one spectrum was collected at each spot, and spectra from nearby spots having similar compositions as seen from the XRF maps were averaged.

Fluorescence-yield Pb-EXAFS spectra of the two hydrogenetic samples AD14, D1-X1 and D21-m3 before treatment and after dissolution of the Mn oxides, as described in Section 2.4, were recorded on the FAME (BM 30B) beamline at the European synchrotron radiation facility (ESRF) in Grenoble, France. The white X-ray beam was collimated vertically to 3 mm with a bent Rh-coated Si mirror, monochromatized with a two-crystal Si (220) monochromator, sagitally focused to 300 μm with the second crystal, and vertically focused to 150 μm with a second bent Rh-coated Si mirror downstream of the monochromator (Hazemann et al., 1995; Proux et al., 2006). X-ray fluorescence was detected with a 30-Ge solid-state detector, and the output signal processed with a fast amplifier (0.125 μs shaping time, 300 eV FWHM resolution). Multiple scans were performed to improve statistics. To avoid the possibility of radiation damage, the sample pellet was moved by 0.5 mm after each scan.

The EXAFS data analysis was carried out using the codes from the WinXAS package (Ressler, 1998). Phase shifts and amplitude functions for the simulation of data were calculated by FEFF7 (Ankudinov and Rehr, 1997) with quenselite as a structural model (Rouse, 1971). The experimental EXAFS function, χ(k), was obtained after subtracting the embedded-atom absorption background from the Pb–Lα fluorescence signal normalized to the intensity of the incident beam (I_0), and normalizing the signal by the edge step. EXAFS spectra were Fourier transformed with a Bessel apodization function to real (R) space, and backtransformed to k space for spectral simulation.

3. Results

3.1. Chemical composition

Abundances of Mn, Fe, Co, Ni, Cu, Zn, and Pb in bulk samples and in the local areas measured by EPMA are listed in Tables 2 and 3. The contents of Co and Pb against

Table 2
Bulk chemical analyses

	Mn (wt %)	Fe (wt %)	Mn/Fe (wt ratio)	Co (mg/kg)	Cu (mg/kg)	Ni (mg/kg)	Zn (mg/kg)	Pb (mg/kg)
D535	12.8	12.7	1.01	4750	1020	2820	465	714
CD25	13.1	12.1	1.08	6350	513	1690	741	1170
AD14	13.4	11.7	1.15	8370	904	3450	1420	1640
D1-X1	5.57	17.1	0.326	830	276	870	441	1650
D21-m3	14.4	13.9	1.04	2450	177	1460	401	1870
G181	29.4	4.68	6.28	1630	11500	8550	1340	162
B6	25.6	5.30	4.83	1140	18800	14300	1310	234
F243-1	26.8	4.20	6.38	1540	12800	10900	1680	211
D513	24.9	5.99	4.16	717	18200	14400	1330	182
D514	20.8	9.30	2.24	1750	9650	10400	908	448
FG352	25.9	6.07	4.27	1320	19200	13300	1170	259
D11-X9	41.6	0.420	99.0	d.l.	13.4	61.0	73.0	35.0
D12-X2	44.2	0.080	553	46.0	4.6	119	54.5	56.0
D21-103	43.2	d.l.	—	176	62.5	295	26.0	34.0
31GTV2-3[a]	12.4	17.2	0.721	755	563	1200	518	408
31GTV6-11[a]	15.4	19.8	0.778	966	713	1730	541	315

d.l., below detection limit.
[a] Data from Kuhn et al. (1998).

the Mn/Fe ratio are plotted in Fig. 1. We know from previous studies (e.g., Moorby and Cronan, 1981; Calvert and Piper, 1984; Aplin and Cronan, 1985a,b; De Carlo and McMurtry, 1992; Usui et al., 1997 Wen et al., 1997) that the Mn/Fe ratio increases, and Co and Pb concentrations generally decrease, from hydrogenetic to diagenetic to hydrothermal Mn formations. Aside from samples 31GTV2-3 and 31GTV6-11, our data are consistent with this general trend, which confirms that the series of samples includes the three genetic types of ferromanganese oxide. The singularity of the two GTV samples, classified as a mixture of hydrogenetic and hydrothermal oxides, is explained by the incorporation of trace elements from seawater (hydrogenetic characteristic) at a fast growth rate (hydrothermal characteristic) (Kuhn et al., 1998).

REE abundances are listed in Table 4, and values normalized to those of the Post-Archean Australian Shale, PAAS (McLennan, 1989) are plotted in Fig. 2a. REE are abundant in hydrogenetic oxides, intermediate in diagenetic oxides, and low in hydrothermal oxides. The Ce anomaly $(Ce/Ce^*)_{SN}$ reported in Table 4 was calculated by defining $(Ce^*)_{SN} = (La^{1/2}Pr^{1/2})_{SN}$ (Akagi and Masuda, 1998), where the subscript SN denotes the abundance normalized to PAAS. The Ce anomaly is referred to as positive ($[Ce/Ce^*]_{SN} > 1$) in hydrogenetic and negative ($[Ce/Ce^*]_{SN} < 1$) in hydrothermal oxides. Diagenetic samples have intermediate values that are close to 1. The decrease in REE abundance and inversion of the Ce anomaly along the hydrogenetic–diagenetic–hydrothermal series is consistent with previous studies (e.g., Usui et al., 1997), confirming that the series of samples is representative of the three genetic types of marine ferromanganese oxide.

3.2. Sequential leaching experiments

The correlation of Co, Ce, and Pb with Fe, and their anti-correlation with Mn in Fig. 1 do not necessarily imply that they are chemically bound to or included in the structure of the Fe oxide component (ferrihydrite). To gain further insight, sequential dissolution experiments were conducted on four hydrogenetic samples (D535, AD14, D1-X1, and D21-m3) and two diagenetic samples (FG352 and G181). The extent of Mn, Co, Ce, and Gd re-adsorption on the Fe oxide after dissolution of the Mn oxide component was evaluated with the multitracer technique on D535 and AD14. Mn and Co were marginally readsorbed (<3%), but Ce ($35 \pm 24\%$) and Gd ($46 \pm 21\%$) were substantially readsorbed.

From 59% (G181) up to 97% (D535 and D1-X1) of total Co, and from 71% (G181) up to 95% (AD14 and D21-m3) of total Mn were leached in fraction 2 (hydroxylamine hydrochloride treatment, Fig. 3), while the ratio of dissolved Fe to total Fe remained low (7–24%). Thus, Mn oxides were preferentially dissolved over Fe oxides during the second extraction step, and this chemical treatment also released most of Co. The Co–Mn association, confirmed below by EPMA and XANES spectroscopy, indicates that the positive Co–Fe/Mn correlation in Fig. 1 is misleading about the nature of the Co host phase. From 75% (D535) to 99% (D21-m3) of total Pb was leached out with Fe in fraction 3 (oxalate treatment). The co-extraction of Pb and Fe in ferromanganese oxides has been interpreted as indicating Pb uptake on Fe oxides (e.g., Koschinsky and Halbach, 1995; Koschinsky and Hein, 2003). This interpretation should be viewed cautiously, however, because Pb is prone to re-adsorption (Gilmore et al., 2001), and this side-effect is expected to be larger than for REE, such as Ce and Gd (Sholkovitz, 1989). Cerium extraction data are conclusive for D535 and D1-X1 because Ce and Mn were eluviated together: 75% Ce and 89% Mn in D535, 62% Ce and 87% Mn in D1-X1. In the other samples, Ce was eluviated predominantly with Fe. Thus, re-adsorption of Mn oxide-bound Ce on Fe oxides may artificially enhance the proportion

Table 3
Electron microprobe analyses (wt%) in main growth structures

Sample name	Mn	Fe	Mn/Fe	Al	Si	P	Ti	Co	Ce	Pb	*N* (number of analyzed points); observed minor phase
D535	20.5–34.4	10.4–22.2	0.92–3.29	0.353–2.10	0.244–2.61	0.109–0.266	0.713–1.15	0.228–1.33	0.134–0.294	0.001–0.169	$N = 30$; Opal with high Fe content
	27.9	16.4	1.81	0.69	0.645	0.217	0.904	0.679	0.208	0.087	
	(3.6)	(3.1)	(0.64)	(0.42)	(0.674)	(0.045)	(0.123)	(0.428)	(0.041)	(0.044)	
CD25	15.5–36.3	9.35–27.8	0.570–3.82	0.044–0.654	0.167–4.40	0.150–0.379	0.829–2.88	0.243–1.32	0.028–0.825	d.l.–0.393	$N = 90$; opal with high Fe content and particle with high contents of Fe and Ti
	26.0	16.5	1.75	0.244	0.919	0.248	1.44	0.648	0.167	0.154	
	(4.5)	(4.5)	(0.67)	(0.147)	(1.13)	(0.055)	(0.45)	(0.352)	(0.093)	(0.104)	
AD14	19.1–39.4	6.47–30.2	0.635–5.81	0.073–0.422	0.043–0.816	0.211–1.88	0.412–1.20	0.168–2.32	0.076–0.260	0.137–0.392	$N = 60$; Phosphate and Fe precipitate (Mn/Fe is around 0.07).
	29.5	16.7	2.64	0.151	0.268	0.561	0.735	0.867	0.152	0.263	
	(6.2)	(8.5)	(1.86)	(0.057)	(0.193)	(0.430)	(0.251)	(0.758)	(0.046)	(0.071)	
D465, inner	18.9–38.2	2.27–15.5	1.27–16.3	0.822–3.96	0.135–2.03	0.047–0.270	0.210–1.07	0.060–0.404	d.l.–0.138	0.019–0.126	$N = 30$
	28.6	9.45	3.96	2.47	0.566	0.141	0.705	0.260	0.077	0.058	
	(4.9)	(3.28)	(3.37)	(0.734)	(0.352)	(0.050)	(0.258)	(0.077)	(0.039)	(0.025)	
D465, outer	16.1–39.7	0.173–18.5	0.955–217	0.755–4.01	0.021–1.30	0.017–0.264	d.l.–0.837	0.001–0.350	d.l.–0.129	d.l.–0.113	$N = 30$
	25.4	8.54	26.4	2.33	0.633	0.135	0.415	0.191	0.059	0.046	
	(8.1)	(6.19)	(51.0)	(0.70)	(0.358)	(0.084)	(0.289)	(0.095)	(0.039)	(0.036)	
D514	23.3–42.8	1.47–3.30	9.14–27.6	0.604–2.24	0.461–1.82	0.036–0.072	0.067–0.749	0.092–0.308	0.111–0.182	n.m.	$N = 7$
	36.3	2.49	15.9	1.54	1.09	0.059	0.265	0.175	0.140		
	(7.1)	(0.60)	(6.59)	(0.66)	(0.50)	(0.013)	(0.289)	(0.095)	(0.027)		
FG352	21.4–46.3	0.103–8.20	3.72–447	0.124–3.38	0.041–3.60	0.021–0.162	0.007–0.453	0.050–0.207	0.052–0.204	n.m.	$N = 7$
	35.8	3.34	100	1.46	1.23	0.076	0.148	0.136	0.119		
	(9.1)	(2.87)	(177)	(1.07)	(1.26)	(0.051)	(0.166)	(0.057)	(0.055)		

First row, range of concentrations; second row, average values, third row (in parentheses), standard deviations of the measured values. In some cases, the standard deviation exceeds the average value due to chemical heterogeneity. d.l., below detection limit; n.m., not measured.

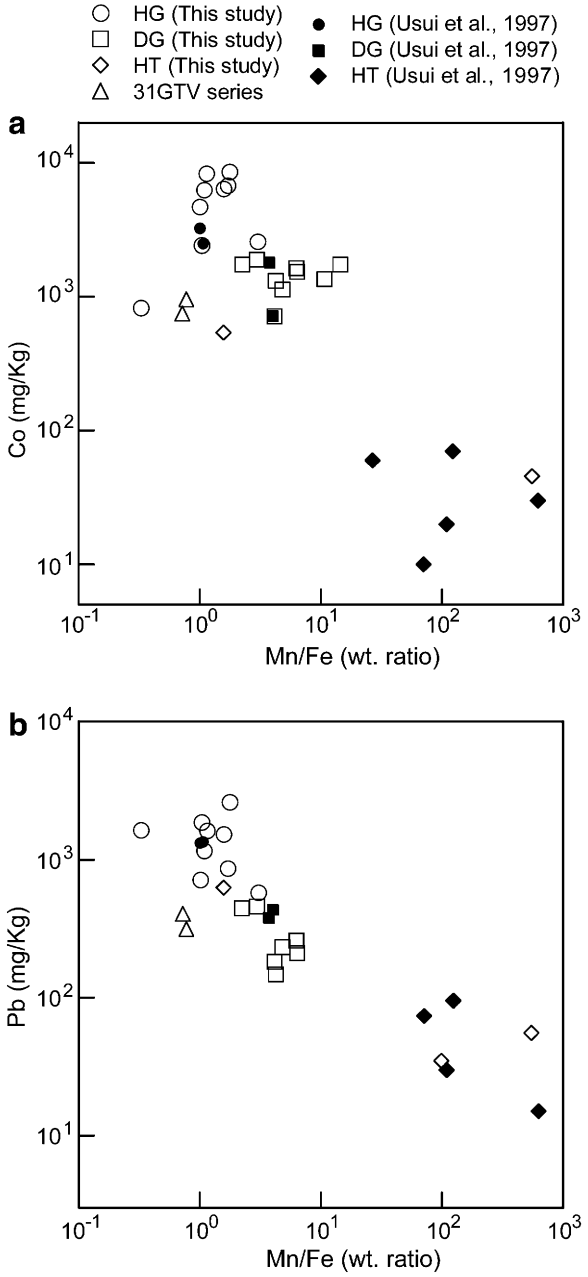

Fig. 1. Co (a) and Pb (b) abundances as a function of the Mn/Fe ratio for the series of ferromanganese oxides studied here and by Usui et al. (1997). Concentrations are from bulk and average EPMA analyses.

of Ce initially held by the Fe phase. Therefore, Ce is at least partly associated with Mn, and perhaps also with Fe.

3.3. Electron microprobe

The micrometer-scale variability of the Co, Ce, and Pb correlations with Fe and Mn was examined by analyzing with EPMA the main growth structures of three hydrogenetic samples (CD25, D535, and AD14). Fair to strong correlations were measured between Co and the Mn to Fe ratio: $r^2 = 0.64$ for CD25, $r^2 = 0.76$ for D535, and $r^2 = 0.80$ for AD14 (Fig. 4). In contrast, Pb and Ce lacked clear correlation with Fe and Mn.

3.4. Cerium L_{III}-edge XANES

The excitation energy of an element increases with its oxidation state, due to an increase in binding energy of core electrons and the destabilization of antibonding states as the formal valency of the metal ion increases (Bianconi, 1988). The chemical shift at the Ce L_{III}-edge is illustrated in Fig. 5 with $CeCl_3$ as Ce(III) reference, and CeO_2, $Ce(OH)_4$ gel, and $Ce(SO_4)_2$ as Ce(IV) references. The trivalent species has an absorption maximum at 5726.5 eV attributed to a single electronic excitation from the $2p_{3/2}$ to the 5d states. The tetravalent species have two maxima at 5730 and 5738 eV attributed to a double electronic excitation in the final states, owing to a strong hybridization of the 4f states of Ce and the ligand orbitals (Jo and Kotani, 1985; Kotani et al., 1987; Soldatov et al., 1994). The absorbance of CeO_2 and $Ce(OH)_4$ is higher at 5730 eV than at 5738 eV, and the two spectra have a shoulder at about 5727 eV. These two features are attributed to many-body effects and to the covalent nature of the Ce–O–Ce bond (Kaindl et al., 1988; Hu et al., 1994; Soldatov et al., 1994; Takahashi et al., 2002a). They are not observed in $Ce(SO_4)_2$ and Ce-sorbed δ-MnO_2 because of the more ionic character of the Ce(IV)–O bond in these compounds (Takahashi et al., 2002a). Apart from D465 (outer), all the sample spectra are similar to those of $Ce(SO_4)_2$ and Ce-sorbed δ-MnO_2, which indicates that Ce is exclusively tetravalent in all genetic-types of ferromanganese oxide. The maximum amount of Ce(III), as estimated from spectral combinations of $CeCl_3$ and $Ce(SO_4)_2$, is 5% for all samples except for D465 (outer).

The previous set of bulk XANES spectra was complemented by a micro-XANES spectrum at a Mn-rich spot (spot 1) and an Fe-rich spot (spot 2) of CD25 (Fig. 6). Spot 1 is within the main growth structure, and spot 2 is in the Fe-rich region on the rim of the main growth structure. From the relative intensities of the Mn K_α and Fe K_β signals, the Mn/Fe ratio at spot 1 is about 5.6 times higher than that at spot 2. EPMA analysis of spot 2 gave 31 wt% Fe, 16 wt% Si, and 0.32 wt% Mn. The Fe–Si association may be due to nontronite (Sorem and Fewkes, 1977; Halbach et al., 1988; Takematsu, 1998). Si may be speciated also as amorphous silica (opal). Regardless of the contrasted chemical composition of the two analyzed spots, their XANES spectra were similar and indicative of Ce(IV) only.

The nature of the main Ce host phase can be inferred from data on the two sorption references. Fig. 5 shows that Ce(III) was oxidized completely to Ce(IV) on δ-MnO_2, but not on ferrihydrite (HFO). The small absorption feature at 5738 eV in the HFO spectra is suggestive of Ce(IV), but this species clearly is minor. Therefore, since Ce is tetravalent in all samples, it should be associated primarily with the Mn oxide component and not, or in subordinate

Table 4
Bulk REE abundances (mg/kg)

Sample name	Y	La	Ce	Pr	Nd	Sm	Eu	Gd	Tb	Dy	Ho	Er	Tm	Yb	Lu	$(Ce/Ce^*)_{SN}$[d]
D535[a]	130	177	1230	41.3	164	38.3	8.97	40.3	5.90	33.8	6.89	20.2	2.88	19.3	2.95	3.31
CD25[a]	188	303	844	70.8	283	62.2	15.1	64.9	9.43	58.0	11.5	32.1	4.39	27.3	4.16	1.33
AD14[a]	131	167	573	28.4	124	25.9	6.58	30.2	4.57	29.2	6.63	20.4	2.90	18.9	3.01	1.91
D1-X1	59.6	203	1130	41.1	168	35.1	8.69	31.8	4.89	23.5	3.94	10.5	1.41	9.23	1.39	2.85
D21-m3	207	304	621	60.3	260	56.5	13.9	61.6	9.68	54.5	10.7	30.3	4.15	25.5	3.90	1.05
D465, inner	115	150	916	33.3	139	30.2	7.38	31.9	5.07	31.0	5.73	18.2	2.59	17.7	2.74	2.98
D465, outer	59.0	63.0	178	18.4	76.7	19.4	4.80	19.2	3.32	18.1	3.41	9.67	1.44	9.51	1.34	1.20
G181	41.4	44.0	91.4	13.6	58.4	14.6	4.13	14.0	2.34	13.2	2.48	6.87	1.01	6.48	0.982	0.860
B6	81.6	68.5	81.7	18.3	79.5	18.8	5.33	19.3	3.22	18.8	3.65	10.7	1.51	9.89	1.53	0.531
F243-1	37.4	36.7	84.8	11.4	49.3	12.6	3.58	12.7	2.14	11.9	2.30	6.44	0.960	6.15	0.939	0.953
D513[b]	64.2	64.4	114	17.2	75.0	17.4	4.21	17.6	2.88	16.5	3.19	9.86	1.31	8.52	1.29	0.790
D514	86.9	103	262	25.6	106	24.3	5.82	25.5	3.85	22.4	4.25	12.0	1.68	11.2	1.64	1.17
FG352	66.9	70.9	64.4	15.4	65.7	15.1	3.43	15.1	2.52	14.1	2.87	9.04	1.21	8.65	1.17	0.448
D11-X9	32.2	4.64	5.14	0.753	3.43	0.776	0.810	1.41	0.261	2.34	0.744	2.85	0.462	3.36	0.617	0.632
D12-X2	12.9	4.24	6.59	0.791	3.68	0.773	0.180	1.08	0.180	1.38	0.370	1.32	0.211	1.60	0.269	0.827
D21-103	1.80	0.661	0.213	0.0839	0.454	0.0590	0.0207	0.103	0.0160	0.133	0.0393	0.127	0.0204	0.152	0.0259	0.208
GTV2-3[c]	189	276	320	61.9	241	48.2	12.2	55.3	7.96	46.8	9.21	25.1	3.68	22.0	3.36	0.563
GTV6-11[c]	186	289	253	60.9	238	48.5	12.1	54.2	7.89	46.8	9.33	25.6	3.74	22.7	3.60	0.439

[a] Data from Takahashi et al. (2000) except for Y.
[b] Average values of six analyses reported in Ohta et al. (1999).
[c] Data from Kuhn et al. (1998).
[d] $(Ce/Ce^*)_{SN}$, the degree of Ce anomaly normalized to PAAS (McLennan, 1989).

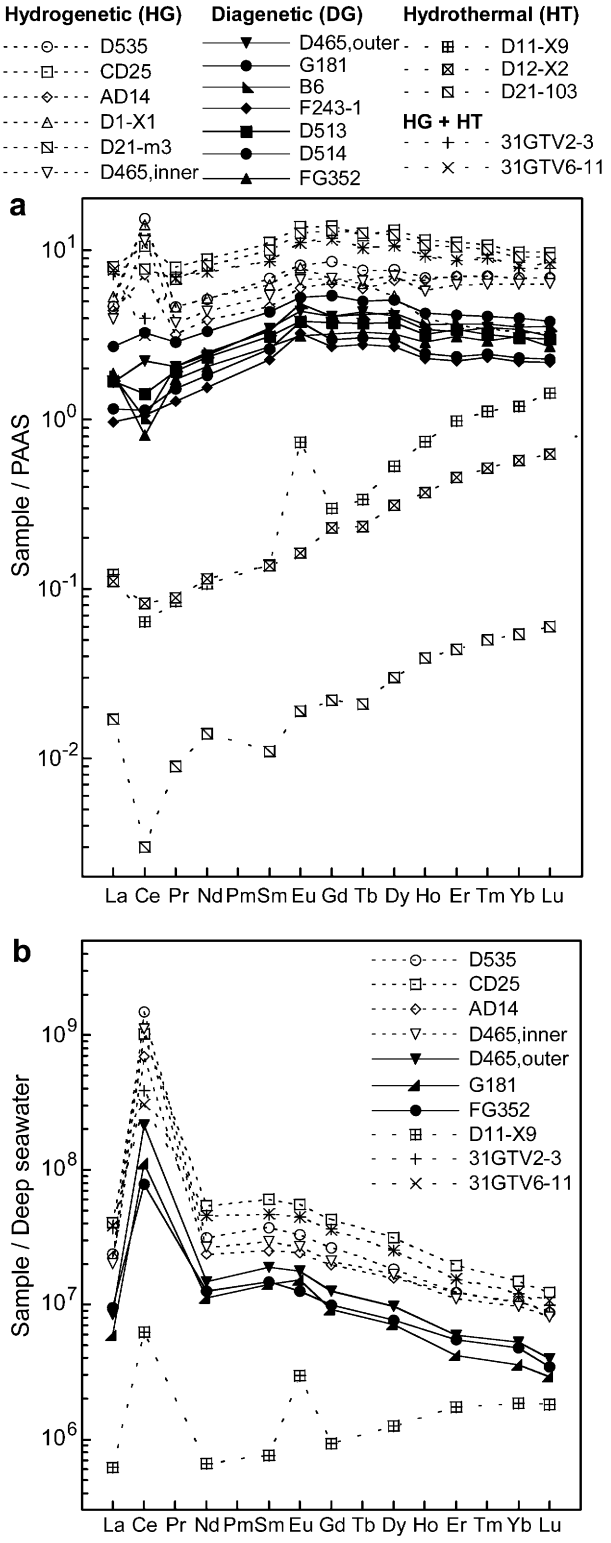

Fig. 2. REE patterns for the three genetic-type ferromanganese oxides. (a) Data normalized to PAAS; (b) data normalized to the average REE abundances in deep seawater (Piepgras and Jacobsen, 1992).

amounts, with the Fe oxide component. This interpretation supposes that ferrihydrite does not oxidize Ce in the physico-chemical conditions of the marine environment, which may not be correct. According to Bau (1999), the ferric oxide reference would have contained more Ce(IV) if sorption had been performed on freshly precipitated colloidal particles rather than on a preformed solid.

3.5. Cobalt K-edge XANES

Fig. 7 shows the Co K-edge XANES spectra of a selection of samples together with those of CoO and Co_2O_3, as references for Co(II) and Co(III), respectively. The chemical shift of the absorption maxima for octahedral Co(II) (7730 eV) and Co(III) (7734 eV) is 4 eV, and can be used to determine the oxidation state of Co in unknown samples (Manceau et al., 1987, 1992a). The sample spectra match the δ-MnO_2 reference, and their edge energy is characteristic of trivalent Co. Two micro-XANES spectra were measured at spots 1 and 2 of CD25 (Fig. 8). From the Co Kα data, the Co concentration is 3.3 times higher at spot 1 than at spot 2. The two point XANES spectra are essentially the same and typical of Co(III). However, a weak shoulder at the energy of the maximum absorbance for the Co(II) species (7729 eV) is apparent on the spot 2 spectrum when the spot 1 spectrum is overlaid. The lineshape of the spot 2 spectrum could be reproduced with a linear combination of 80–85% spot 1 + 10–15% CoO. This result provides suggestive evidence for some Co–HFO association, but the data are too noisy to draw a definitive conclusion. Therefore, we conclude that Co is trivalent in hydrogenetic (CD25, D465 inner), diagenetic (G181, D465 outer), and hydrothermal (D21-103) Mn oxides. Similarly to Ce, the non-oxidation of Co(II) at the ferrihydrite surface in contact with air, and its oxidation on δ-MnO_2 (Fig. 7), provide strong evidence for Co association to the Mn oxide component.

3.6. Lead L_{III}-edge XANES

Fig. 9a shows the Pb L_{III}-edge XANES spectra of a selection of hydrogenetic (CD25, D1-X1, D465 (inner), and D21-m3) and diagenetic (D465 (outer) and G181) ferromanganese oxides, and the two sorption (HFO, δ-MnO_2) and the PbO, Pb_3O_4, and PbO_2 references. The spectra from the natural and synthetic samples resemble the PbO spectrum. Since Pb-XANES spectra are essentially featureless, first derivatives are generally plotted to enhance the spectral sensitivity to the electronic structure of Pb (Rao and Wong, 1984; Bargar et al., 1997a; Choi et al., 1999). The 2p to 6s electronic transition at 13.029 keV is possible for the Pb(IV) species owing to its $(5d)^{10}(6s)^0$ configuration, but not for Pb(II), since the two 6s electronic levels are filled in this species. The 2p → 6s transition is absent in all spectra from natural and synthetic samples, which indicates that Pb is divalent in marine ferromanganese oxides, and that no oxidation occurred upon Pb sorption on HFO and δ-MnO_2, in agreement with previous experimental studies (Manceau et al., 1992b; Bargar et al., 1998; Matocha et al., 2001; Trivedi et al., 2003; Villalobos et al., 2005). As Pb is dissolved as a divalent species, such

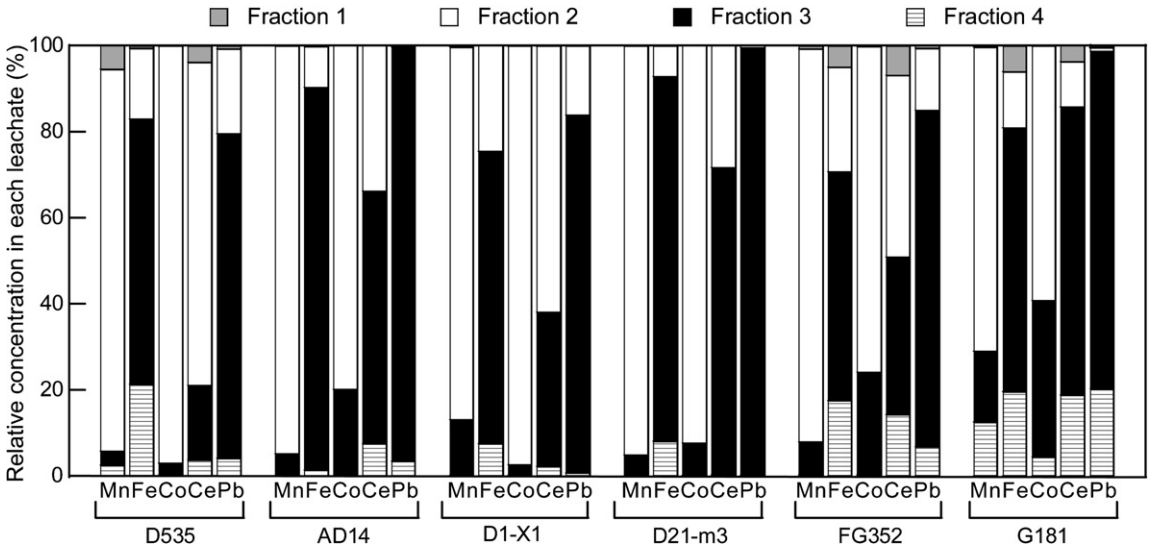

Fig. 3. Results from sequential dissolution of D535, AD14, D1-X1, and D21-m3 (hydrogenetic), and FG352 and G181 (diagenetic) ferromanganese oxides. Metal speciation has been operationally defined by Koschinsky and Halbach (1995) and Koschinsky and Hein (2003) as follows. Fraction 1: exchangeable cations and Ca carbonate fraction; fraction 2: Mn oxide fraction; fraction 3: Fe oxyhydroxide fraction; fraction 4: residual fraction, mainly consisting of silicates and aluminosilicates.

as $PbCl_n^{2-n}$ and $PbCO_3^0$, in seawater (Byrne, 2002), and as many redox reactions are catalyzed at mineral surfaces (Wehrli, 1990), it has been conjectured that the oxidation of Pb(II) to Pb(IV) is the main enrichment mechanism of Pb in marine ferromanganese oxides (Goldberg, 1965; Hem, 1978; Murray and Dillard, 1979; Nishimura, 1983; Halbach et al., 1988). This hypothesis is not supported by our data.

Since Pb is not oxidized by Mn oxides, XANES data do not allow determining whether Pb is associated with the Fe or Mn oxide component. Based on sequential extraction data, Pb is associated with Fe, but this macroscopic technique for determining metal speciation has pitfalls, as mentioned previously. To answer this question, the three hydrogenetic samples AD14, D1-X1 and D21-m3 were examined by EXAFS spectroscopy.

3.7. Lead L_{III}-edge EXAFS

3.7.1. Pb mineral host

The mineralogical nature of the Pb host in AD14, D1-X1 and D21-m3 was determined by recording the EXAFS spectra of the untreated and hydroxylamine hydrochloride treated (fraction 2) samples. The spectra can be classified in three groups on the basis of their shape and frequency: AD14, D1-X1 and D21-m3, and the three treated samples (Fig. 10a–e). The spectra within each of the second and third groups are statistically invariant, as illustrated in Fig. 10b with D1-X1 and D21-m3. These two spectra could be reconstructed with a linear combination of untreated AD14 and either of the treated samples (Fig. 10f). Consequently, the whole data set forms a binary system which is bounded by AD14 and the Mn-free samples (fraction 2). Comparison of the fraction 2 spectra with Pb-sorbed Fe (oxyhydr)oxides references from a database showed that the treated spectra matched best the ferrihydrite spectrum (PbHFO100), (Fig. 11a and b). This result is consistent with chemistry and diffraction data, since Fe is speciated as ferrihydrite in these samples.

The nature of the Pb host in AD14 was determined by comparing its spectrum with those from the Pb-sorbed δ-MnO_2 references. The PbdBi112 spectrum provided the best match to the data (Fig. 11c and d). The ferromanganese and reference spectra are similar, differing only in the shape of the ascending part of the second oscillation. Qualitatively, one may conclude that Pb has a similar binding environment, and hence likely occupies the same crystallographic sites, in the natural and synthetic phyllomanganates. This interpretation is supported by the Fourier transforms, which show that Pb has a similar local structure in the two solids. Linear combinations of Mn and Fe (oxyhydr)oxide references verified that Pb is associated only with the Mn oxide phase in AD14, with a detection limit for Pb-ferrihydrite estimated at 10%. Since AD14 and the fraction 2 spectra are from pure species, the fractional amounts of Fe- and Mn-bound Pb in D1-X1 and D21-m3 can be estimated from their spectral reconstruction with the two single species spectra. The best fits to the D1-X1 and D21-m3 spectra were obtained with $50 \pm 10\%$ Mn-bound Pb and $47 \pm 10\%$ Fe-bound Pb (Fig. 10f).

3.7.2. Uptake mechanism of Pb

The nature of the polyhedral connectivity between Pb and the $Fe(O,OH)_6$ octahedra in ferrihydrite was determined by least-squares fitting the reference rather than the sample data because the former had a higher signal-to-noise ratio. The Fourier transform of PbHFO100 exhibits a Pb–O peak at $R + \Delta = 1.8$ Å and a Pb–Fe peak

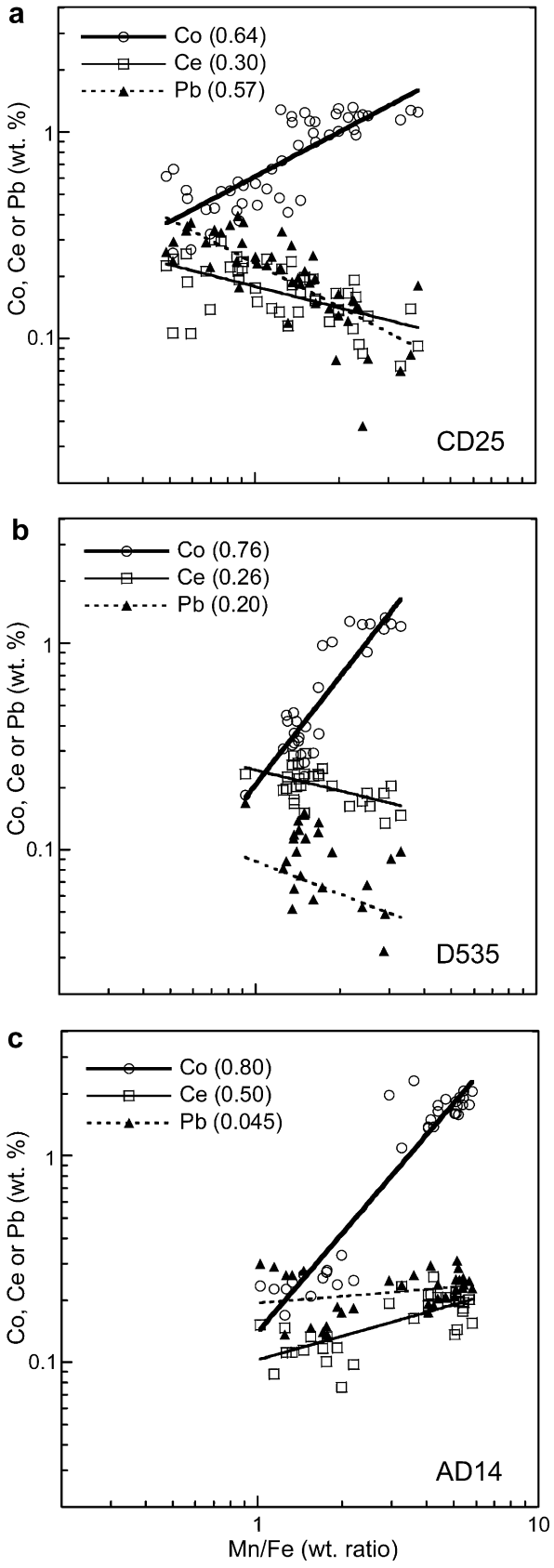

Fig. 4. Co, Ce, and Pb abundances against Mn/Fe ratio in CD25, D535, and AD14. Data from electron microprobe analyses. Numbers in parenthesis are correlation coefficients (r^2).

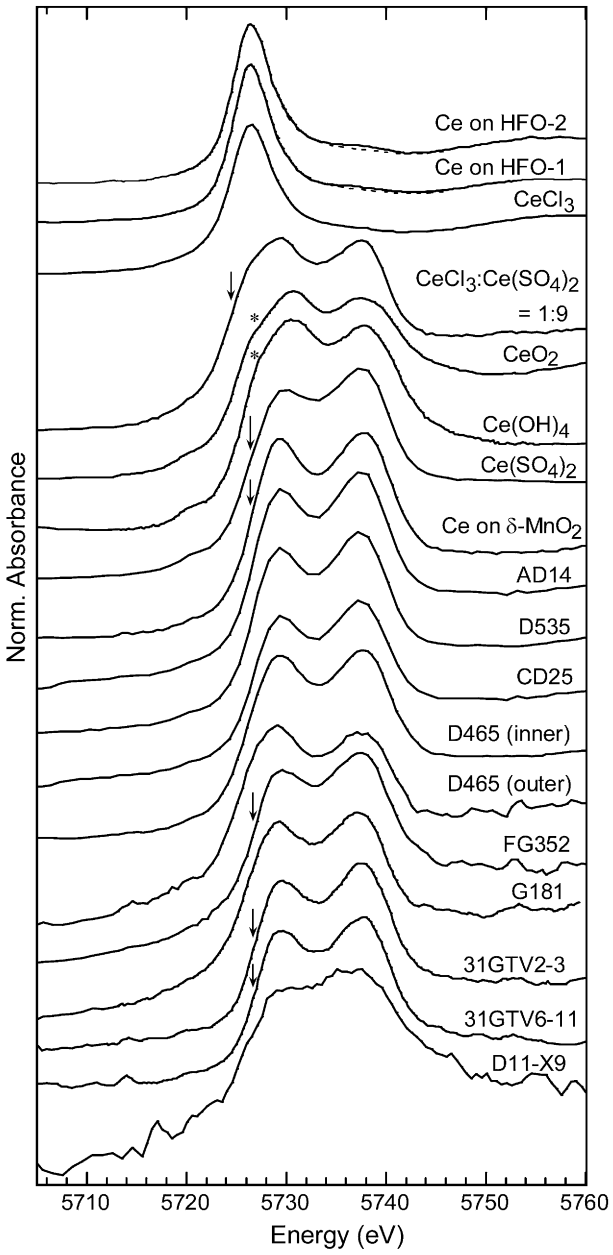

Fig. 5. Cerium L_{III}-edge XANES spectra of a selection of ferromanganese oxides and references. Ce-sorption reaction times are 1 h on δ-MnO_2 and HFO-1 and 120 h on HFO-2. An overlay plot of the $CeCl_3$ spectrum is represented in dotted line for comparison. In some spectra, the position of the maximum of the 1st derivative is indicated by an arrow. CeO_2 and $Ce(OH)_4$ have a shoulder at 5727 eV pointed out by an asterisk.

at $R + \Delta = 2.9$–3.0 Å, or $R \sim 2.3$ Å and 3.3–3.4 Å, respectively, after semi-quantitative correction of the phase-shift effect (Manceau et al., 1992b; Ford et al., 1999; Scheinost et al., 2001; Trivedi et al., 2003) (Fig. 11b). More precise interatomic distances were obtained from spectral fits. The best fit structural parameters derived from a two-shell fit model were 2.8 O atoms at 2.36 Å and 1.6 Fe at 3.39 Å (Fig. 12a; Table 5). This model failed to reproduce the wave node at 4.8 $Å^{-1}$ and the shape of the third oscillation at 7 $Å^{-1}$. Splitting the first oxygen shells in two subshells moderately improved the simulation, but splitting the iron

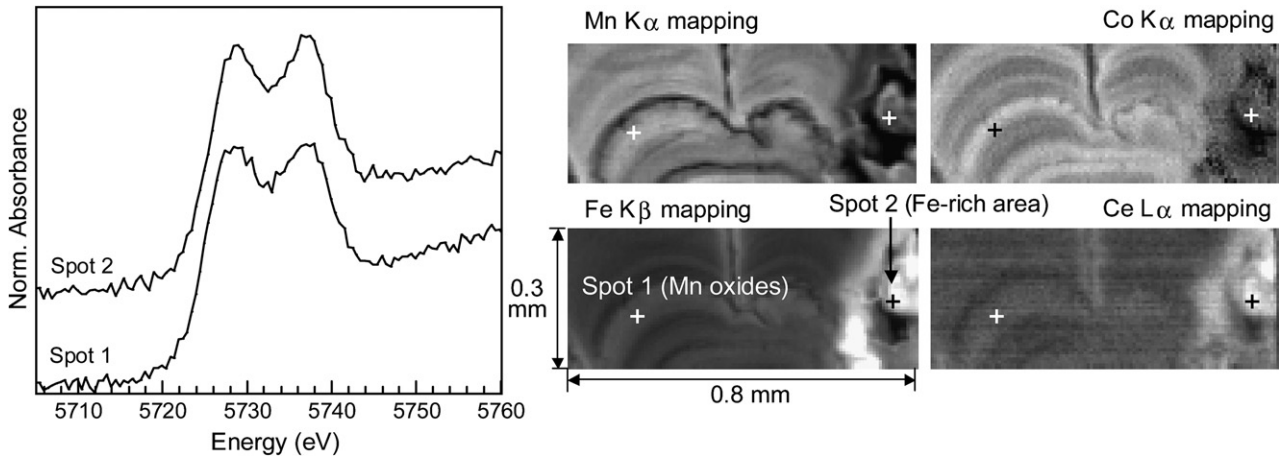

Fig. 6. Cerium L_{III}-edge micro XANES spectra at spot 1 in the growth structure and at spot 2 in the Fe-rich area of CD25. The locations of the analyzed spots are indicated by a cross in the X-ray fluorescence maps. White = high concentration.

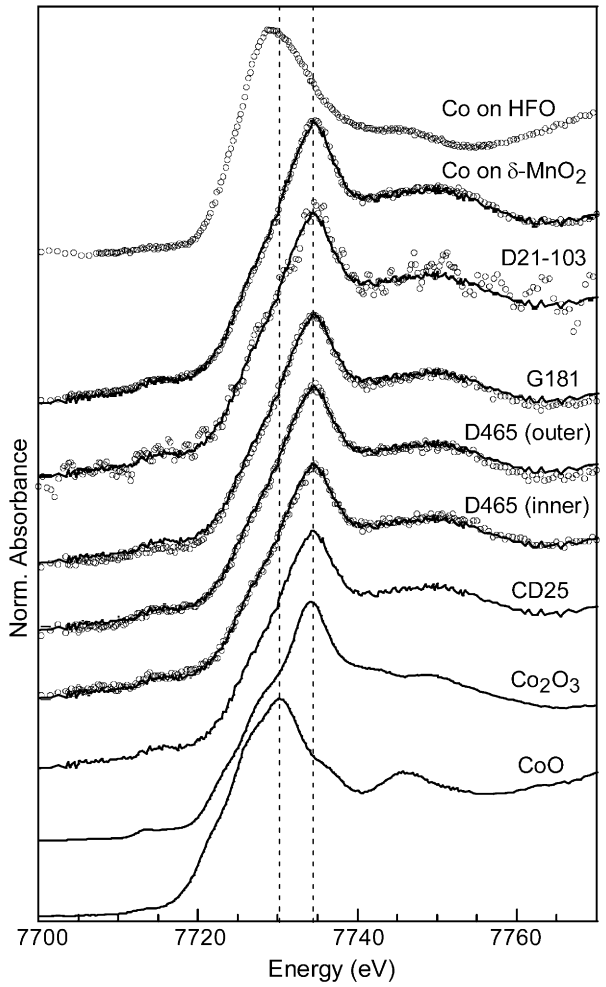

Fig. 7. Cobalt K-edge XANES spectra of a selection of ferromanganese oxides and references. The CD25 spectrum is plotted over the spectra of D465 inner and outer, G181, D21-103, and Co sorbed on δ-MnO_2 to guide the eyes.

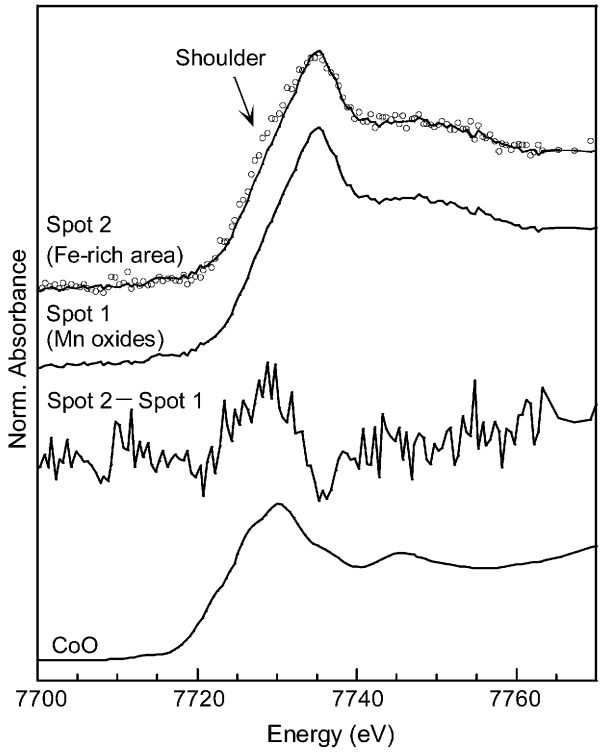

Fig. 8. Cobalt K-edge micro XANES spectra at spots 1 and 2 on the X-ray fluorescence map presented in Fig. 6. The difference spectrum suggests that 10–15 % of Co is divalent at spot 2.

shell improved it quite significantly as it halved the goodness-of-fit parameter (Fig. 12b–d, Table 5). An optimal fit to the data was obtained with a four-shell model consisting of about 3 O at 2.38 Å, 1 O at 2.65 Å, 2 Fe at 3.32 Å and 2 Fe at 3.50 Å (Fig. 12d). The Pb–O distances are characteristic of divalent Pb (Manceau et al., 1996), and the Pb–Fe distances of a bidentate edge-sharing complex (ES) between the Pb and Fe coordination polyhedra.

In contrast to ferrihydrite, the Pb-metal shell peak is a doublet (Mn1 and Mn2) in the Fourier transform of AD14 (Fig. 11d), which is evidence for at least two Pb–Mn distances. Since the two Pb–Mn peaks are weak, the geometry of the Pb surface complex and nature of the sorption site in AD14 were determined from the analysis of the

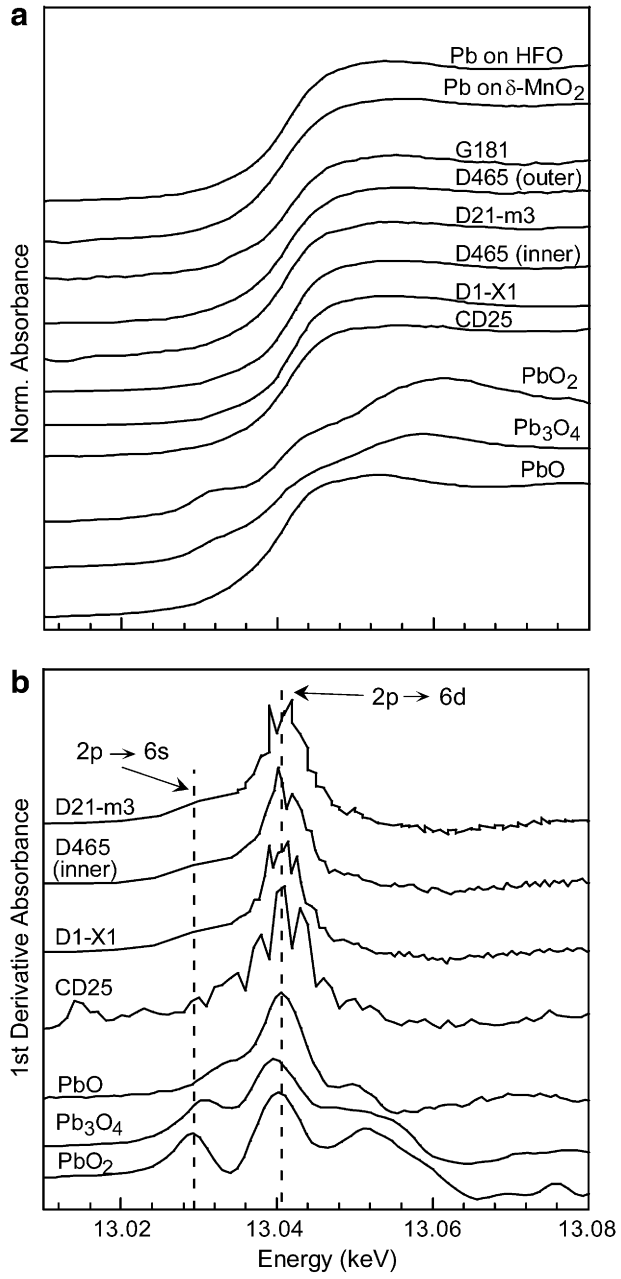

Fig. 9. (a) Lead L_{III}-edge XANES spectra of hydrogenetic and diagenetic ferromanganese oxides and reference compounds. (b) First derivative of some XANES spectra.

Pb sorption reference spectra. The five phyllomanganate spectra intersect at the same k values, which signifies that the system is binary (Manceau et al., 1998), and thus that the local structure of Pb varies continuously between two well-defined configurations (Fig. 13a). On the Fourier transforms, the Mn2 peak has a high amplitude and the Mn1 peak a weak amplitude at high surface loading in the δ-MnO_2 series, and even more so in well-crystallized birnessite (PbBi31). Decreasing the surface loading down to Pb/Mn = 0.002 (sample PbdBi2) on δ-MnO_2 increased the amplitude of the Pb–Mn1 peak and concomitantly decreased that of the Pb–Mn2 peak (Fig. 13b). The dependence of the relative amplitude of the two Pb–Mn peaks on the Pb/Mn ratio and crystallinity demonstrates the presence of two surface complexes having a different affinity for the phyllomanganate surface, as shown previously for Zn on phyllomanganate (Manceau et al., 2002a; Toner et al., 2006) and Cd on goethite (Spadini et al., 1994). When the surface coverage is low and the surface area high (i.e., δ-MnO_2), the short distance Pb species prevails, meaning that it has a high affinity for the mineral surface, while it is outnumbered by the long distance and lower affinity Pb species at high surface coverage.

Good spectral agreement between theory and experiment for the δ-MnO_2 series was obtained by considering only one shell of oxygens at 2.3 Å and two Mn shells (Mn1 and Mn2) at 3.2 and 3.7 Å (Fig. 12; Table 5). The Mn1 shell has been observed previously in δ-MnO_2 and manganite (γ-MnOOH), and was interpreted as an edge-sharing (ES) complex (Matocha et al., 2001; Morin et al., 2001). In ferrihydrite, in which the ES complex also occurs, the Pb–Fe interaction is about 0.1 Å larger (i.e., 3.3 Å) than the Pb–Mn interaction in δ-MnO_2, a value that matches the difference in effective ionic radii between Mn(IV) and Fe(III) (0.53 vs 0.64 Å). Since δ-MnO_2 has a layered structure and its crystallites have a small lateral extension (i.e., low crystallinity), the ES complex is located probably at layer edges and is presumably tridentate (Fig. 14). The Mn2 shell has been reported previously in well-crystallized birnessite and attributed to a tridentate corner-sharing complex (TCS) in the interlayer (Manceau et al., 1999, 2002a; Morin et al., 1999; Matocha et al., 2001). This structural interpretation was confirmed subsequently by electron and X-ray diffraction (Drits et al., 2002; Lanson et al., 2002a). At this interlayer position, the Pb atoms are bonded to three O atoms from a vacant octahedral site of the Mn oxide layer, thus helping to balance the charge deficiency of the layer created by Mn(IV) vacancy sites (Fig. 14).

Consideration of a Mn3 shell at 4.09 Å in PbBi31 better replicated the data than the single Mn2 shell model, in particular in the $9 < k < 11$ Å^{-1} interval (Fig. 12k, Table 5). This second shell was not resolved in our previous study (Manceau et al., 2002a) because the EXAFS data were limited to $k < 10$ Å^{-1}. The magnitude of the distance separation between the Mn2 and Mn3 shells (4.09–3.70 = 0.39 Å) is similar to that in quenselite (3.96 – [(3.57 + 3.43)/2] = 0.46 Å; $PbMnO_2OH$) (Rouse, 1971) and, by analogy with the structure of this mineral, the six nearest Pb–Mn distances from the TCS complex likely are unequal. The incoherency of the Pb–Mn distances in Pb-sorbed birnessite explains the apparent loss of coordination since an effective number of $N = 1.0 + 0.8 = 1.8$ Mn atoms are detected instead of a crystallographic number of $CN = 6$ (Fig. 14).

Another distinction among the reference spectra is a 0.04 Å reduction of the average Pb–O distance in PbBi31 and PbdBi197 relative to PbdBi2, PbdBi44, and PbdBi112 (Table 5). Since the first group of samples has a higher ES/TCS ratio, the ES complex presumably has a longer

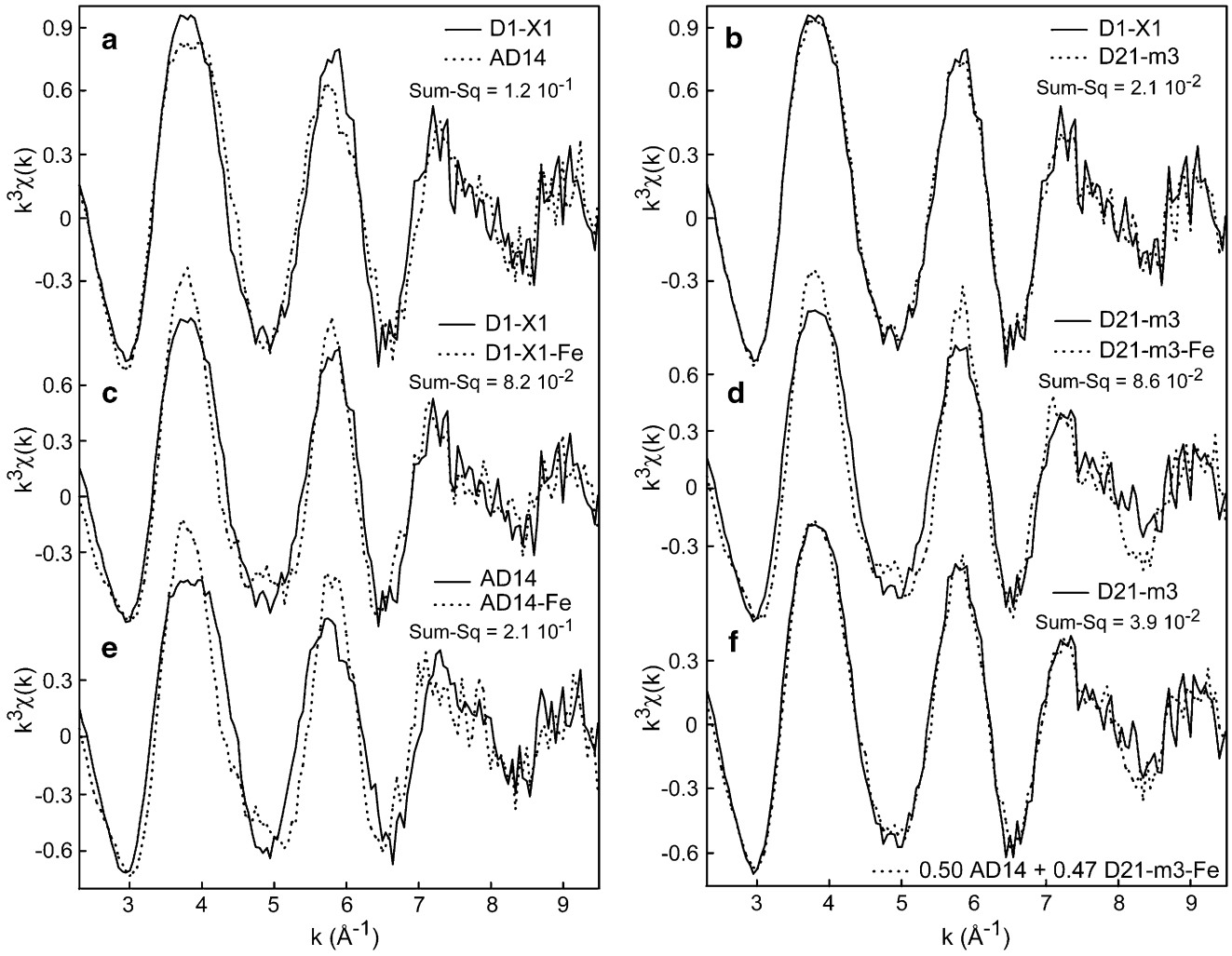

Fig. 10. Pb L_3-edge EXAFS spectra of untreated (D1-X1, AD14 and D21-m3) and hydroxylamine-treated (D1-X1-Fe, AD14-Fe and D21-m3-Fe) hydrogenetic ferromanganese oxides (a–e). The D21-m3 spectrum was best simulated (Sum-sq = 0.039) with a mixture of AD14 and D21-m3-Fe, in proportions of 50% and 47 %, respectively. Precision: 10% of total Pb (f).

average Pb–O distance than the TCS complex. This increase in distance can be explained by the higher electrostatic repulsion between Pb(II) and Mn(IV) at the edge-sharing site (shorter Pb–Mn distance) than at the corner-sharing site (longer Pb–Mn distance). This effect was detected because the proportion of TCS complex is low at low surface coverage.

Finally, the proportion of ES and TCS complexes in AD14 was estimated from the effective number of Pb–Mn1 and Pb–Mn2 pairs ($N = 0.2$ and 0.6, respectively; Table 5) and the crystallographic number of nearest Mn neighbors at site TCS ($CN = 6$) and ES ($CN = 2$) (Fig. 14). According to this calculation, Pb is evenly distributed over the two sites.

4. Discussion

4.1. Ce anomaly

Cerium L_{III}-edge XANES data showed that Ce is exclusively tetravalent in all samples, regardless of genetic origin. In general, Ce oxidation is considered to be responsible for the positive Ce anomaly in REE patterns of ferromanganese oxides (e.g., Takahashi et al., 2000). The rationale is that Ce(IV) is taken up preferentially over Ce(III) by solid phases in contact with seawater because Ce(IV) is much less soluble than Ce(III). This explanation does not seem to be valid for diagenetic and hydrothermal ferromanganese oxides because they have a negative, or at best moderately positive, Ce anomaly when the data are normalized to PAAS (shale), as is often observed (Fig. 2a). Fig. 2b shows that this discrepancy disappears when the REE concentrations in the solid phase are normalized to their abundances in deep seawater (Piepgras and Jacobsen, 1992). In doing this, the Ce anomalies are all positive, which agrees with the dominance of Ce(IV) in all samples (Fig. 2b). The reason is that REE in deep seawater, where hydrogenetic nodules occur, are more strongly depleted in Ce than the more reducing interstitial and hydrothermal waters, where the two other types of ferromanganese oxides occur. Also, Ce normalization by PAAS is unsuitable

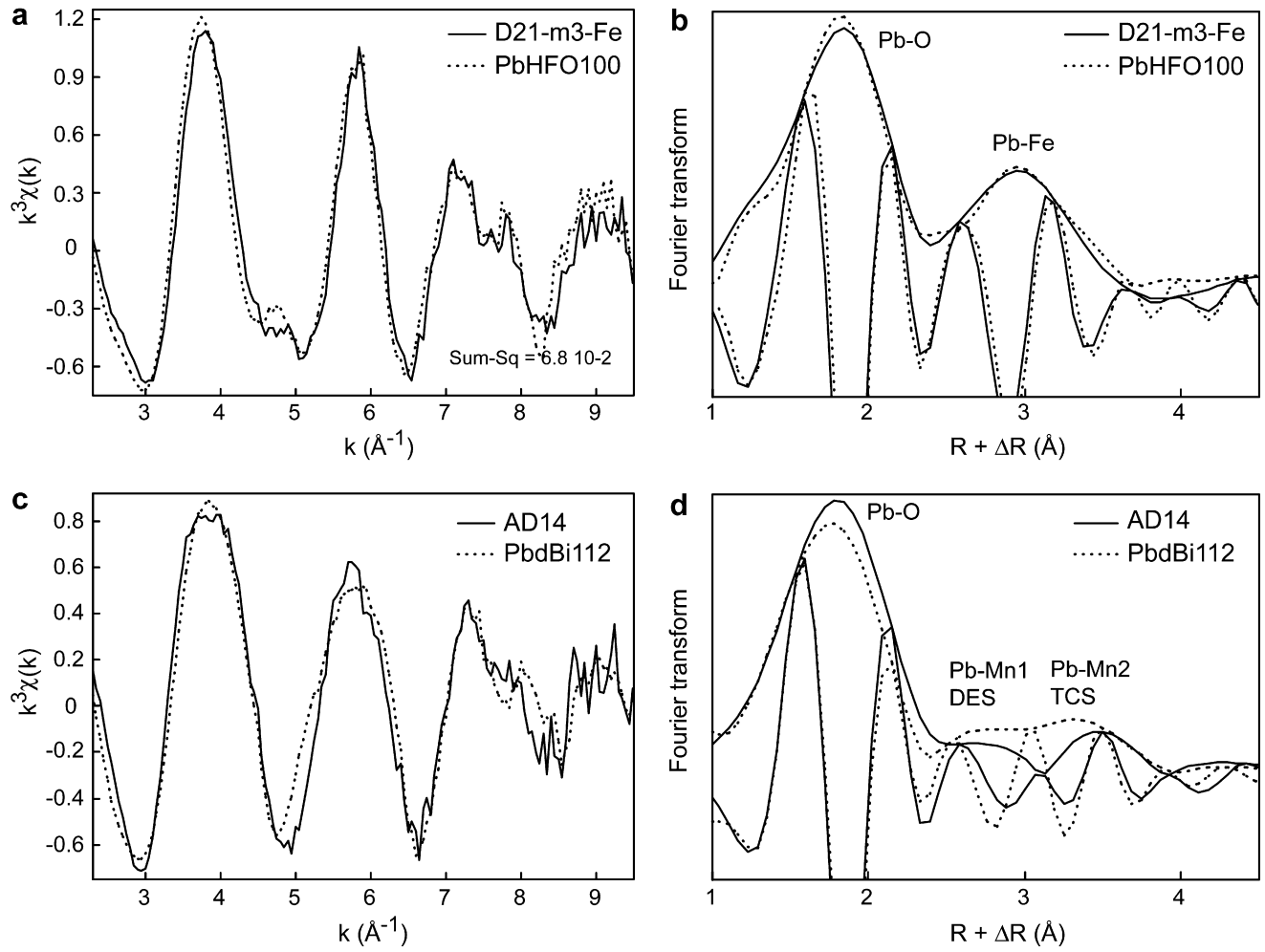

Fig. 11. Pb L_3-edge EXAFS spectra (a,c) and Fourier transforms (b,d) of hydroxylamine-treated D21-m3 (D21-m3-Fe) and untreated AD14 compared to Pb-sorbed ferrihydrite (PbHFO100, pH 6.5) and Pb-sorbed δ-MnO_2 (PbdBi112, pH 5) references. The numbers after the code names are the Pb to sorbent metal (Fe or Mn) mole ratio in parts per thousand.

because Ce is not removed by the same geochemical processes in shales and marine nodules.

If we assume that Ce(III) in ferromanganese oxides is in equilibrium with Ce(III) in water, and that Ce(III) is the only soluble species, then the normalized abundance of Ce(III) in the solid phase, denoted Ce*, can be obtained from the interpolation of the normalized abundances for La and Pr: $(Ce^*)_{SW} = (La^{1/2}Pr^{1/2})_{SW}$, where SW stands for normalization by REE abundances in seawater. The $(Ce^*/Ce_{total})_{SW}$ ratio calculated for FG352 is 15%, and could be detected by XANES spectroscopy. This ratio is a maximum value among the samples examined, because this sample has the lowest Ce anomaly in the dataset (Fig. 2b). The $CeCl_3$:$Ce(SO_4)_2$ spectrum in Fig. 5 shows that 10% of Ce(III) in a mixed-valence sample manifests itself in the appearance of a shoulder at 5724 eV. None of the sample spectra have such a shoulder including FG352. Also, the maximum of the 1st derivative of this composite spectrum is at 5724.4 eV, while this maximum is between 5726 and 5727 eV in the sample spectra and Ce(IV) references. This analysis confirms the lack of detectable Ce(III) in ferromanganese oxides, even in a sample having a weak Ce anomaly. Therefore, Ce(III) is completely oxidized to Ce(IV) in ferromanganese oxides, and the magnitude of the positive Ce anomaly is not related to a variation of redox conditions, but probably to kinetic factors, as discussed below.

4.2. Ce and Co incorporation in ferromanganese oxides

Homogeneous precipitation and formation of Ce oxide in marine sediments have been proposed for Ce(IV) removal from seawater (e.g., De Carlo and McMurtry, 1992; Ohta et al., 1999; Haley et al., 2004). This mechanism can be dismissed because none of the XANES spectra of the samples resemble those of CeO_2 and $Ce(OH)_4$. Therefore, oxidative sorption of dissolved Ce(III) likely is the main pathway of Ce incorporation in ferromanganese oxides. Since Ce(IV) is sparingly soluble (De Baar et al., 1988; Byrne, 2002), the sorbate remains at the surface of the Fe–Mn oxide after oxidation took place, leading progressively to Ce enrichment. Based on the low amount of

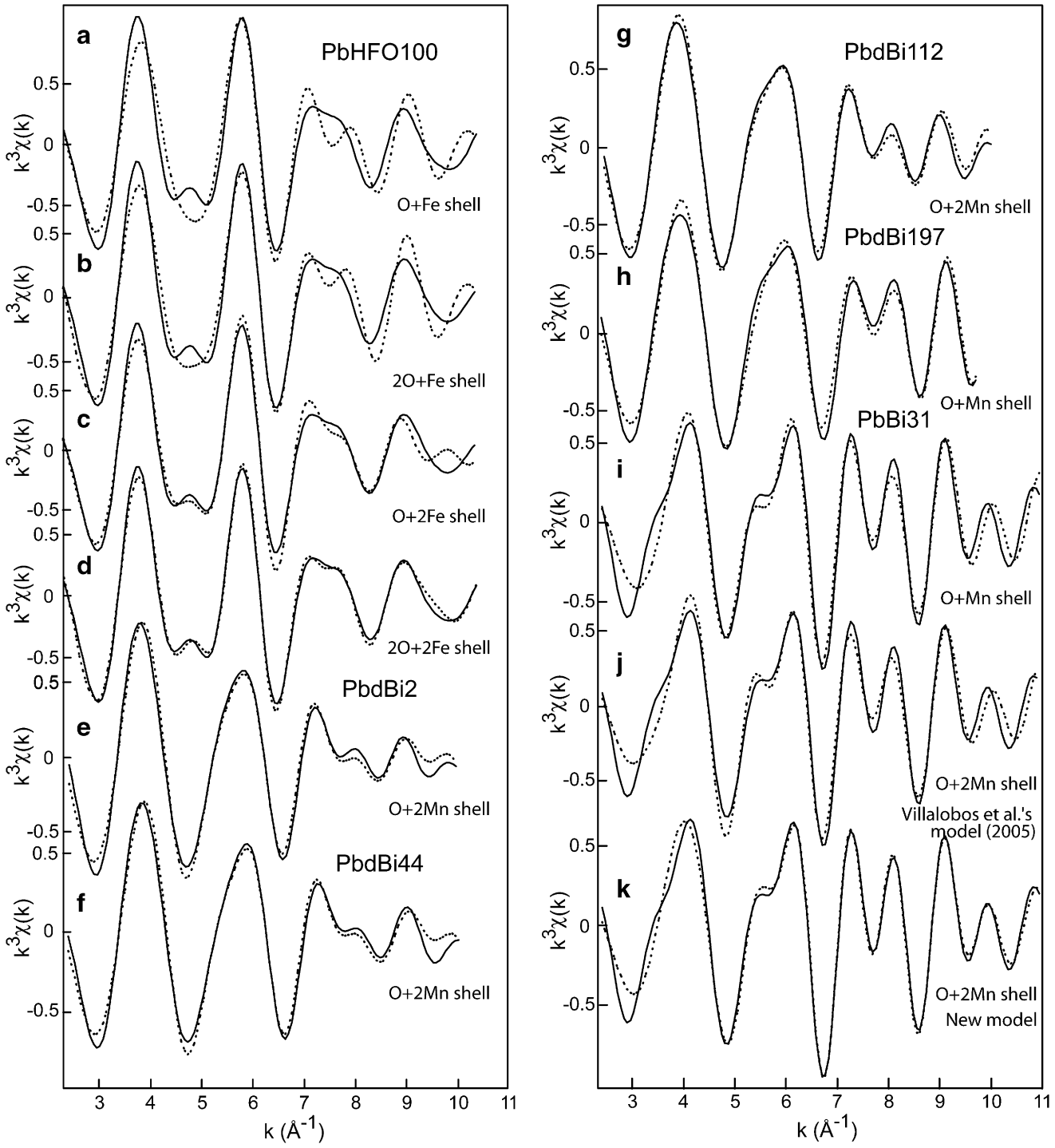

Fig. 12. Model fits of the Pb-EXAFS data for lead sorbed on ferrihydrite (PbHFO), δ-MnO_2 (PbdBi) and well-crystallized birnessite (PbBi). The data are in solid lines, and the models in dashed lines, and the best-fit parameters for each model are listed in Table 5. The contributions from the Pb–O, Pb–Fe (ferrihydrite), and Pb–Mn (δ-MnO_2 and birnessite) nearest shells have been filtered by Fourier transformation.

Ce in seawater and the nanometer size of the ferrihydrite and manganese particles (Villalobos et al., 2006), saturation of reactive surface sites by Ce(IV) is unlikely to occur. Also, the exposed surface is progressively buried during the growth of the ferromanganese oxide. This process controls the Ce enrichment, and prevents poisoning of the surface, as observed in the laboratory at high sorbate–metal sorbent ratio (Manceau et al., 1997). Therefore, Ce enrichment must be controlled by the growth rate of the ferromanganese oxide, as suggested for Co (Halbach et al., 1983; Mannheim and Lane-Bostwick, 1988; Takematsu et al., 1989). Consistent with this interpretation, the growth rate of ferromanganese oxides increases in the order hydrogenetic < diagenetic < hydrothermal oxides (Dymond et al.,

Table 5
Pb-EXAFS for Pb sorbed phyllomanganates and hydrous ferric oxide

Sample	Fit Model	O shell			Me[a] shell			ΔE_0 (eV)	*Rp*
		R (Å)	*N*[b]	σ^2 (Å^2)	*R* (Å)	*N*[b]	σ^2 (Å^2)		
PbBi31	Two-shell fit	2.30	1.6	0.011	3.72	1.3	0.008	−5	24
	Three-shell fit	2.29	1.7	0.012	3.70	1.0	0.008[c]	−9	14
					4.09	0.8	0.008[c]		
	Three-shell fit[d]	2.29	1.7	0.011	3.46	1[e]	0.014	−7	24
					3.70	3[e]	0.014		
PbdBi197	Two-shell fit	2.29	2.3	0.012	3.68	0.8	0.008	−9	15
PbdBi112	Three-shell fit	2.33	2.2	0.012	3.23	0.2	0.008[c]	−9	12
					3.73	0.6	0.008[c]		
PbdBi44	Three-shell fit	2.33	2.3	0.012	3.23	0.3	0.008[c]	−9	15
					3.73	0.5	0.008[c]		
PbdBi2	Three-shell fit	2.34	2.2	0.012	3.25	0.3	0.007[c]	−9	15
					3.76	0.5	0.007[c]		
PbHFO100	Two-shell fit	2.36	2.8	0.013	3.39	1.6	0.014	−4	32
	Three-shell fit	2.37	2.9	0.013[c]	3.41	1.6	0.014	−2	26
		2.66	1.2	0.013[c]					
	Three-shell fit	2.36	2.9	0.013	3.26	1.9	0.014[c]	−5	17
					3.44	2.7	0.014[c]		
	Four-shell fit	2.38	3.3	0.014[c]	3.32	1.9	0.014[c]	−1	9
		2.65	1.3	0.014[c]	3.50	2.5	0.014[c]		

EXAFS parameters were optimized by minimizing the *Rp* value (%) defined as sum $\{|k^3\chi_{exp} - k^3\chi_{fit}|\}$/sum$\{|k^3\chi_{exp}|\}$. The $R + \Delta$ intervals for the Fourier backtransforms were [1.1–4.2] Å for PbBi31, [1.1–3.9] Å for PbdBi197 and PbdBi112, [1.1–3.8] Å for PbdBi44 and PbdBi2, and [1.1–3.7] Å for PbHFO100.
[a] Me = Mn for Mn compounds, and Me = Fe for HFO.
[b] Effective coordination numbers. The Pb full coordination is lost due to anharmonic structural disorder.
[c] σ parameters constrained to the same value for the two sub-shells. $S_0^2 = 0.85$.
[d] Same model fit as Villalobos et al. (2005).
[e] Parameters fixed to the same values as in Villalobos et al. (2005).

1984), while the degree of Ce anomaly (and REE content) decreases in the reverse order. The fact that the Fe/Mn ratio varies with the Ce anomaly does not mean that Ce is associated with the Fe oxide component.

This geochemical interpretation of the Ce partitioning at the Mn oxide–water interface can be extended to cobalt, since this element is divalent in seawater (Byrne, 2002), oxidized to Co(III) by Mn oxides (Murray and Dillard, 1979), sparingly soluble in its oxidized form, systematically present as Co(III) in the three genetic-type oxides, and less abundant in fast growing ferromanganese oxides (Halbach et al., 1983; Mannheim and Lane-Bostwick, 1988). Co(III) is substituted isomorphically for Mn in the manganese layer (Manceau et al., 1987, 1997), and the steric match between Co(III) (0.54 Å) and Mn(IV) (0.53 Å) is believed to be responsible for the selective enrichment of cobalt in manganese oxides (Burns, 1976). The nature of the Ce incorporation site in phyllomanganates is unknown. With a size of 0.80 Å in octahedral coordination, Ce(IV) is too big to occupy Mn layer site, but may reside in the interlayer on top of vacant Mn layers sites commonly observed in metal-containing birnessite (Drits et al., 2002; Lanson et al., 2002a; Manceau et al., 2002a).

4.3. Pb surface complexation on ferrihydrite

EXAFS results show that Pb forms the same type of surface complex on marine ferrihydrite as in the laboratory. Pb sorption on synthetic ferrihydrite at pH 6.5 was modeled by Manceau et al. (1992b) by two nearest oxygen subshells at 2.22 and 2.42 Å, and two next-nearest iron subshells of 0.3 Fe at 3.29 Å and 0.4 Fe at 3.45 Å. The two Pb–O (2.38 and 2.65 Å) and Pb–Fe (3.32 and 3.50 Å) distances reported here are similar to those inferred in our past spectroscopic study. The new values are more accurate because the Pb-EXAFS spectrum from the previous study had a lower signal-to-noise ratio and *k* range. The Pb–O distances are similar to those in β-PbO (2.21 and 2.49 Å; Leciejewicz, 1961) and, by analogy with the coordination of Pb(II) in this compound, lead atoms are assumed to be at the apex of a distorted pyramid. The Pb–Fe distances are interpreted by the formation of an ES surface complex, and their bimodal distribution as the consequence of the split of the Pb–O distances in the first shell. Similar geometry was reported for lead sorption on goethite and hematite (Bargar et al., 1997b, 1998). The formation of an ES complex on synthetic ferrihydrite was confirmed by Scheinost et al. (2001), who reported an Fe coordination about Pb of one at a distance of 3.32 Å at pH 5.0. In this last study, the local structure of Pb was invariant with the reaction time (up to 2 months), ferrihydrite morphology (with and without freeze-drying), metal competition (Cu^{2+}), and fulvic acid concentration. Similarly, Trivedi et al. (2003) reported an average Pb–Fe distance of 3.34 Å on ferrihydrite at pH 5.5 and 6.5. While the resolution in interatomic distance was lower in the studies of

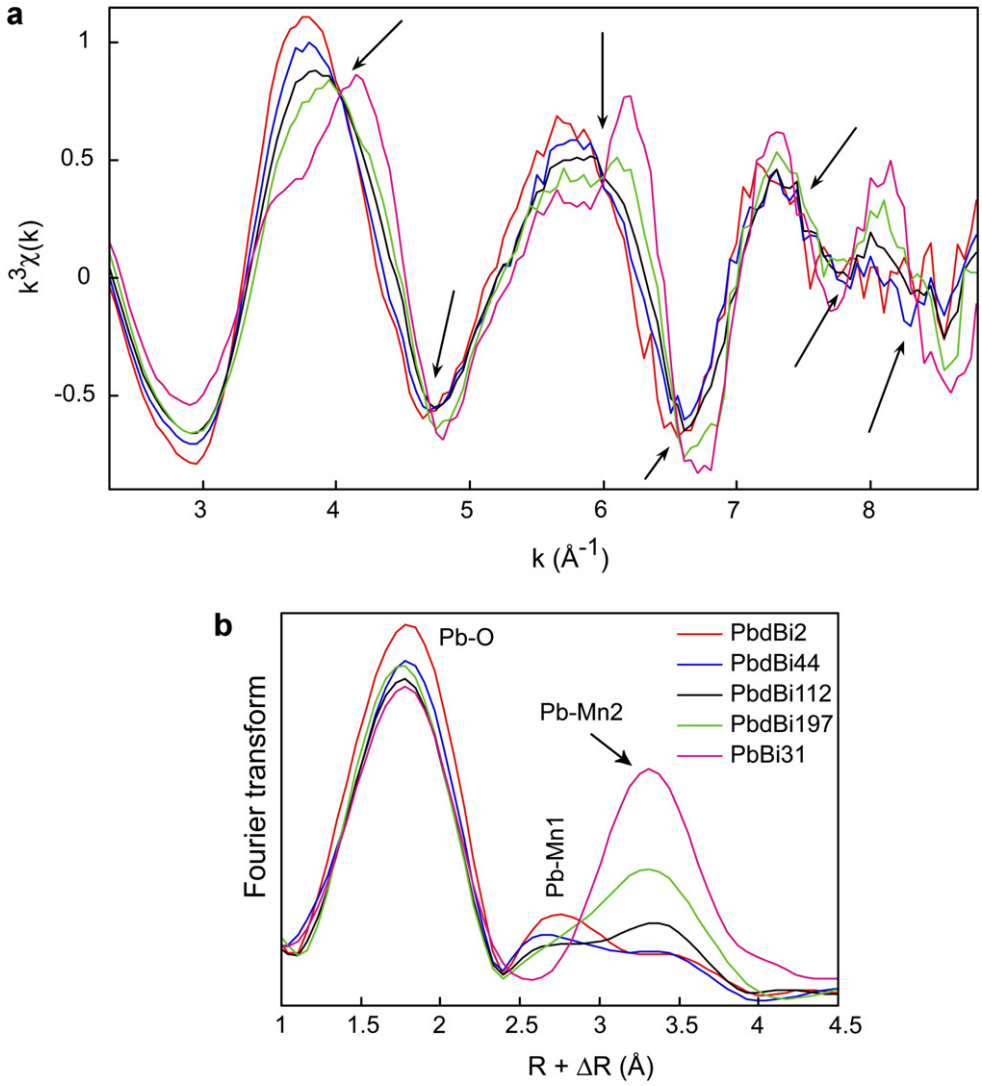

Fig. 13. Pb L_3-edge EXAFS spectra (a) and Fourier transforms (b) of Pb sorbed on δ-MnO_2 (PbdBi series) and well-crystallized birnessite (PbBi) at different Pb/Mn ratio.

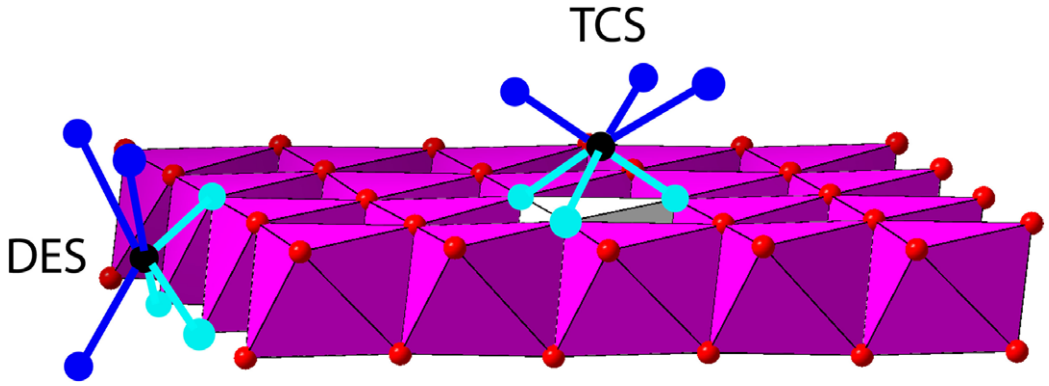

Fig. 14. Structural model for the uptake mechanism of Pb on Mn^{3+}-free phyllomanganate. TCS and DES are triple-corner and double-edge sharing complexes. At low surface loading, Pb occupies both lateral (DES) and basal (TCS) sites of the MnO_2 layer. On the lateral site, the base of the Pb pyramid is formed by two conjoined edges from two neighboring Mn(IV) octahedra (tridendate edge-sharing complex). On the basal site, the base of the Pb pyramid is formed by the face of a vacant Mn(IV) layer octahedron and, therefore, is parallel to the layer plane (tridendate corner-sharing complex).

Scheinost et al. (2001) and Trivedi et al. (2003), all of the above results collectively support the formation of edge-sharing lead complex on ferrihydrite, regardless of its origin and formation conditions. In particular, there is no spectroscopic evidence for the existence of Pb–Cl pairs in natural samples and, hence, for the formation of a Pb–Cl–Fe ternary surface complex, despite the high activity of chlorine (0.54 M) in seawater. This finding was predicted from laboratory studies (Balistrieri and Murray, 1982; Bargar et al., 1998).

4.4. Pb surface complexation on phyllomanganate

Two short distance Pb–Mn pairs were identified, one at 3.2 Å and another at 3.7 Å, corresponding to ES and TCS complexes, respectively. The ES complex occurs at layer edges (Morin et al., 2001) and the TCS complex in the interlayer (Manceau et al., 1999, 2002a,b; Morin et al., 1999; Matocha et al., 2001). The detection of the ES complex at low Pb loading in δ-MnO_2 indicates that it has a high affinity for the phyllomanganate surface. This complex likely occurs in PbBi31, but its fractional amount relative to the TCS complex is negligible because PbBi31 contains 15 times more Pb than PbdBi2, and its particles have a larger lateral size (i.e., better crystallinity). Their lateral dimension, as estimated by X-ray diffraction from the size of coherent scattering domains (CSD), is ~200 Å (Lanson et al., 2002a) compared to 60 Å for δ-MnO_2 (Villalobos et al., 2003), consistent with Brunauer–Emmett–Teller (BET) measurements, showing that the well-crystallized birnessite particles have an external (N_2) specific surface area of 27 m^2/g (Manceau and Charlet, 1992) vs. 120–150 m^2/g for δ-MnO_2 (Villalobos et al., 2003).

The higher affinity of lead for lateral sites cannot be explained by a higher number of Pb–O–Mn bonds at these sites since in the proposed structural model (Fig. 14) lead is coordinated to three surface oxygens on both interlayer and external sites (i.e., formation of a tridentate complex on both sites). The reason may be electrostatic in nature. Because the three oxygens from a vacant octahedral site are doubly coordinated to layer Mn, the total charge deficit at a TCS site is $3\times[(-2)+2\times(4^+/6)]=-2$ v.u. Thus, sorption of two protons or one Pb^{2+} at a TCS site compensates the charge deficit on either side of a Mn(IV) vacancy (Silvester et al., 1997). In contrast, the ES site has two oxygens singly coordinated to bulk Mn atoms and one doubly coordinated (Fig. 14). The total charge at an ES site is $2\times[(-2)+(4^+/6)]+[(-2)+2\times(4^+/6)]=-3.3$ v.u. Its charge compensation requires the sorption of one Pb^{2+} and one or two protons. Then, the high reactivity of lateral sites towards metal sorption can be viewed as the consequence of the lamellar structure of δ-MnO_2 and the nanometer size of the particles (high external to internal surface ratio). One may argue that basal sites should be preferred over lateral sites since conjoined edges have significantly more Pb^{2+}–Mn^{4+} repulsion (shorter Pb–Mn distance) than TCS sites. However, lateral sites have less steric restriction than basal sites because two of the three surface oxygens are singly coordinated in the first case, whilst they are all doubly coordinated in the second.

4.5. Evaluation of the formation of DCS complexes at layer edges

The progressive reduction in amplitude of the TCS Pb–Mn peak (d(Pb–Mn2) = 3.7 Å) with decreasing Pb/Mn ratio (Fig. 13b) is interpreted as the preponderance of a high surface-affinity ES complex (d(Pb–Mn1) = 3.2 Å) at low surface coverage. This evolution also has been interpreted by the existence of a double-corner sharing (DCS) complex on layer edges with a Pb–Mn distance of 3.50–3.55 Å (Villalobos et al., 2005). In this alternative model, the TCS and DCS sites were supposed to be occupied concurrently and independently of the Pb/Mn ratio, meaning that Pb had the same affinity for external (DCS) and internal (TCS) sites. As explained below, this structural interpretation is problematic.

In the DCS + TCS model of Villalobos et al. (2005), the data were fit with the following assumptions. First, Pb forms a DCS complex ($CN = 2$) at layer edges and a TCS complex ($CN = 6$) in interlayers. This predetermined structural model was used in the spectral simulations to constrain the EXAFS numbers (N) of Mn neighbors at each site to the Pb occupancy (f_{ext} and f_{int}, with $f_{ext}+f_{int}=1$), such that $N(\mathrm{DCS})=2\times f_{ext}$ and $N(\mathrm{TCS})=6\times f_{int}$. For example, if Pb was evenly distributed among the two sorption sites, then $N(\mathrm{DCS})=2\times0.5=1.0$, and $N(\mathrm{TCS})=6\times0.5=3$. Second, the structural disorder is anharmonic in the O shell ($N(\mathrm{EXAFS}) < CN$) and harmonic in the Mn shells ($N(\mathrm{EXAFS}) = CN$). This assumption is incorrect for the immense majority of Pb compounds, including sorption complexes (Manceau et al., 1996; Bargar et al., 1997a). In practice, this model reproduced the data fairly well (Fig. 12j), but with generally meaningless values (e.g., $\sigma = 0.16$ Å) for the Debye–Waller parameter (the harmonic model becomes questionable when σ is higher than ~0.10 Å; Teo, 1986; Crozier, 1997). With one exception this disorder parameter was arbitrarily fixed to a lower value for the more distant TCS shell than for the DCS shell, as if the structural disorder in solid matter could decrease with radial distance. Still another problem with the DCS + TCS model is the unrealistically large interval of variation of the energy threshold parameter ($-21 \leqslant \Delta E_0 \leqslant -13$ eV). In a binary system, this parameter should be constant, both for physical reasons and to decrease the degree of freedom (Schlegel et al., 2001), otherwise non-linear least-squares fits converge to local minima and, hence, to erroneous structural solution.

Consequently, the physical and mathematical problems with the DCS + TCS model are believed to be the reasons for the misidentification of the ES complex at 3.2 Å as a DCS complex at 3.50–3.55 Å. To test this hypothesis, the PbBi31 spectrum was fit successively with the TCS

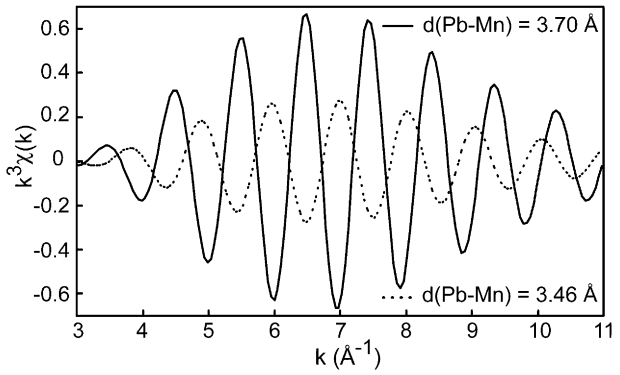

Fig. 15. Electronic waves from the two Mn shells at $R = 3.46$ ($N = 1.0$, $\sigma^2 = 0.014$ Å^2) and $R = 3.70$ Å ($N = 3.0$, $\sigma^2 = 0.014$ Å^2) for PbBi31 in the model fit of Pb-sorbed phyllomanganate proposed by Villalobos et al. (2005). The two waves are out-of-phase at 6.5 Å^{-1} ($\Delta E_0 = 0$ eV).

(Fig. 12i) and the DCS + TCS (Fig. 12j) models. This sample contains major TCS and minor ES complexes because it has 15 times more Pb than PbdBi2, and its particles have a large lateral dimension. The TCS model ($R = 3.72$ Å, $N = 1.3$, $\sigma^2 = 0.008$ Å^2) and the DCS + TCS model ($R = 3.46$ Å, $N = 1.0$, $\sigma^2 = 0.014$ Å^2 + $R = 3.70$ Å, $N = 3.0$, $\sigma^2 = 0.014$ Å^2) equally reproduced the data ($Rp = 24$, Table 5), and accounted for the major spectral features. This apparently anomalous result has a simple explanation.

Consider an EXAFS signal consisting of waves from two shells as in the DCS + TCS model, with the shells differing only in distance and coordination number. A simplified representation of this signal is given by

$$\chi = A(k)\exp(2ikR + \delta(k))(1 + a\exp(2ik\Delta r))$$

where A and δ are the usual single-scattering EXAFS terms, a is the ratio of amplitudes of the two shells, R the distance for the stronger shell (TCS), and Δr the distance difference. In our case, $a = 1/3$ since $f_{ext} = f_{int}$, $R = 3.70$ Å, and $\Delta r = -0.24$ Å. For these values, the phase difference $2k\Delta r$ is π at $k = 6.5$ Å^{-1} and, the two waves interfere destructively over most of the data range (Fig. 15). This makes the coordination number appear small, and the FT peak low in amplitude. However, it is not obvious that the sum of the two waves really looks like a single wave. We can show that it does by considering the phase difference between the combined signal (DCS + TCS model) and that from a single wave (TCS model) with distance R:

$$\Delta\phi = \arg(1 + a\exp(2ik\Delta r))$$

If we draw an Argand diagram (phasor plot), we see that as a function of k, this phase difference oscillates between limits of $\pm \sin^{-1}a$, which is about 19° (0.34 rad) here. The extrema occur when $2k\Delta r = \pi \pm (\pi/2 - \sin^{-1} a)$. In our case, $\Delta R = 0.24$ Å, so these points occur at $k = 4$ and 9.1 Å^{-1}, approximately bracketing the range where the signal is largest. Thus, within that range, there is an approximately linear phase difference between the DCS + TCS and TCS-only signals, which can be compensated for in the data fitting by adjusting the assumed distance (i.e., 3.70 vs. 3.72 Å) and energy origin (i.e., $\Delta E_0 = -7$ vs -5 eV, Table 5). The above argument even accounts for the distance in the TCS model fit (3.72 Å) being greater than the greater of the two distances in the DCS + TCS model (3.70 Å). The phase difference $\Delta\phi$ is negative for $k < \pi/(2\Delta R)$, zero at $k = \pi/(2\Delta R)$, where the shells are exactly out of phase, and positive for $k > \pi/(2\Delta R)$, which is the effect provided by a distance increase over R, plus a small adjustment of the energy origin ΔE_0. Similarly, the amplitude can be shown to be approximately (within the goodness of the fit to TCS-only) described by a change of mean-square relative deviation (i.e., σ value). We see that unless the data are taken over a large k-range and fit to very good models, it can be impossible to tell the difference between a single shell (TCS model) and a pair of shells (DCS + TCS model) of different coordination numbers and distances. Here, the correct model (ES + TCS) was determined by varying experimentally the Pb/Mn ratio over two orders of magnitude ($0.002 < \text{Pb/Mn} < 0.197$ in the δ-MnO_2 series) compared to a factor of 5 ($0.035 \leqslant \text{Pb/Mn} \leqslant 0.174$) in Villalobos et al. (2005), and by constraining the variation range of the fit parameters to physically meaningful values.

4.6. Pb partitioning among Mn and Fe oxide

With a Mn/Fe weight ratio of 1.04 (Table 2) and a Mn- to Fe-bound lead ratio of approximately 1, lead is unfractionated between the two oxides in D21-m3. In contrast, it is moderately partitioned in the Mn oxide in D1-X1 (Mn/Fe = 0.3; Mn-bound/Fe-bound ≈1), and strongly partitioned in AD14 (Mn/Fe = 1.1; Mn-bound/Fe-bound > 9). The sorption of Pb on both Fe and Mn oxide in D21-m3 and D1-X1 can be explained by the fact that conjoined edge sites also exist at chain terminations in ferrihydrite (Drits et al., 1993) which also have a high affinity for cations (Spadini et al., 1994). Therefore, tridentate sites at chain terminations in Fe oxide and at layer edges in Mn oxide may sorb lead equally in marine ferromanganese oxides. The similarity of the O–O conjoined edge distances for FeO_6 octahedra (2.59 Å; Szytula et al., 1968) and MnO_6 octahedra (2.62 Å; Lanson et al., 2002b) also explains the ability of the two oxides to complex Pb(II) adions in tridentate edge-sharing geometries. Fe oxides may also bind metal adions in bidentate edge-sharing geometries (i.e., sharing of only one edge with a single octahedron), but apparently the energy stabilization gained from forming multiple edge bonds to the Fe oxide surface is higher (Spadini et al., 2003). In summary, from a structural standpoint, lead may sorb on either oxide, and its strong partitioning in AD14 does not have a simple structural explanation.

It has been suggested that lead is associated with the Fe oxide component in marine ferromanganese oxides because Pb is speciated as neutral or negatively charged moieties, such as $Pb(CO_3)_n^{(2-2n)^-}$ ($n > 1$) and because Fe oxides have a net positive charge and Mn oxides a net negative charge at circumneutral pH (Stumm, 1993; Koschinsky and Halbach, 1995; Langmuir, 1997; Koschinsky and Hein,

2003). This electrostatic explanation to geochemical partitioning on Fe oxide is satisfying for anionic species, such as AsO_3^{3-} and AsO_4^{3-} (e.g., Smedley and Kinniburgh, 2002; Koschinsky and Hein, 2003), but not for Pb because cationic moieties (Pb^{2+}, $PbCl^+$, and $PbOH^+$) co-exist with neutral and negative species in seawater according to chemical equilibrium calculations. Three explanations can be proposed for Pb sorption on Fe and Mn oxides in seawater. First, cationic lead species preferentially sorb on Mn oxide and anionic lead species on Fe oxide. Second, sorption of cationic Pb species on Mn oxide shifts chemical equilibrium in direction of the dissociation of anionic Pb complexes, thus leading to Pb enrichment on Mn oxide. Third, the chemical (i.e., binding) component of the free energy for tridentate Pb(II) sorption to octahedral edges on both oxides is much larger than the electrostatic component. In this case a charged adion is sorbed specifically regardless of the sign of the surface charge (Anderson and Rubin, 1981). Since Pb can be taken up by Mn and Fe oxides in the marine environment, the Pb–Fe/Mn correlation in Fig. 1b does not mean that Pb is chemically bound to the Fe oxide component, but that its enrichment depends on the growth rate of the ferromanganese oxide, as for Ce and Co.

Independent of the geochemical partitioning of Pb between Mn and Fe oxide, both oxides have strong binding sites that must be able to retain Pb over long periods of time because ferromanganese deposits have a slow growth rate (mm/Myr) (e.g., Halbach et al., 1983, 1988; Takematsu, 1998). Knowing the molecular mechanism of Pb sequestration in these deposits is essential to understand its marine geochemistry, and in particular its enrichment by up to a factor of 200 relative to its crustal abundance (8.0 mg/kg; Faure, 1998) and 7×10^8 relative to seawater concentration (1.3×10^{-11} M; Schaule and Patterson, 1981). This knowledge is also important for environmental contamination issues because ferrihydrite and vernadite (the generic term for natural turbostratic phyllomanganate; Manceau et al., 2006) are ubiquitous in soils and continental sediments (Chukhrov and Gorshkov, 1981; Dixon and Skinner, 1992; Davison, 1993; Manceau et al., 2003, 2005; Vodyanitskii and Sivtsov, 2004; Hochella et al., 2005a), and because the lead-ferrihydrite/lead-vernadite co-association (D21-m3, D1-X1) and the lead-vernadite partitioning (AD14) described here are common (McKenzie, 1989; Hudson-Edwards, 2000; Latrille et al., 2001; Liu et al., 2002; Cornu et al., 2005; Hochella et al., 2005b). Therefore, this work provides context for further studies on the sequestration mechanism of Pb at Earth's surface.

4.7. Redox reactions of Ce, Co, and Pb sorbed on ferromanganese oxides

Although Co and Ce have similar geochemical behavior in the marine environment (Addy, 1979; Ohta et al., 1999), some differences exist that are related to their redox properties. Ce and Co are both readily oxidized by manganates, but while Ce may be oxidized also by Fe oxyhydroxides (e.g., Bau, 1999; Kawabe et al., 1999), Co is not (e.g., Coughlin and Stone, 1995; Angove et al., 1999; Jeon et al., 2003; Pozas et al., 2004). The redox potential of the Ce(III)/CeO_2 couple in seawater is about Eh = 178–237 mV ($p\varepsilon = 3$–4; De Baar et al., 1988). The redox potential of the Co^{2+}/CoOOH couple at pH 8, $Co^{2+}_{(aq)} = 2.0 \times 10^{-11}$ M (the dissolved Co concentration in seawater; Martin et al., 1989), and $E^0 = 1.48$ V (Moffett and Ho, 1996), is 689 mV. Thus, Ce(III) is easily oxidized in seawater, even by dissolved oxygen (De Baar et al., 1988), whereas Co(II) is only oxidized by MnO_2 (Murray and Dillard, 1979; Manceau et al., 1997).

Thermodynamic considerations also help understand the lack of oxidation of Pb(II) to Pb(IV) in marine ferromanganese oxides. The potential of the Pb^{2+}/PbO_2 couple is 837 mV, based on Brookins (1988, data) and a $Pb_{(aq)}$ concentration in seawater of 1.3×10^{-11} M (Schaule and Patterson, 1981). This value is greater than the potential of H_2O/O_2 at $P_{O_2} = 1$ atm and pH 8 (756 mV), meaning that Pb(II) cannot be oxidized to Pb(IV) in homogeneous condition within the stability field of water. Catalytic Pb(II) oxidation at the phyllomanganate surface could occur (Murray and Dillard, 1979), but XANES and EXAFS spectroscopic data show that it does not (Matocha et al., 2001; Manceau et al., 2002a; Takahashi et al., 2002b; Villalobos et al., 2005). According to thermodynamic calculations, Pb(II) oxidation could be mediated by hausmannite (Mn_3O_4; Hem, 1978), but this mixed-valence Mn oxide with a spinel structure has never been identified in marine ferromanganese oxides.

Thus, it can be argued that the partitioning of the three redox-sensitive trace metals depends on their redox potential. Since Co(II) is oxidized exclusively by Mn(III) and Mn(IV), and is present as Co(III) in marine ferromanganese oxides, then this element can be anticipated to be strictly associated with Mn oxides, as is shown by ample experimental evidence. Ce, which is immobilized also in its oxidized form, probably is associated predominantly with Mn oxides because Mn(IV) is a strong oxidant at pH 8.3. However, Ce(IV)–Fe oxide associations may also occur, as Ce(III) can be oxidized by oxygen and freshly precipitated Fe oxides (Bau, 1999). This association is not widespread because it is inhibited kinetically by the slow rate of Ce(III) to Ce(IV) oxidation by O_2 and Fe(III). Of the three trace metals studied here, Pb probably has the lowest affinity for Mn oxides, since it is always divalent. This hypothesis is supported by EXAFS data, which show that Pb is associated partly with Fe in two of the three samples examined, and re-adsorbed on the Fe component when the Mn component is dissolved. The lesser affinity of Ce and Pb for the Mn oxide component compared to Co likely accounts for the weak Ce–Mn/Fe and Pb–Mn/Fe correlations measured by EPMA (Fig. 4). Consistent with our hypothesis, the correlation between Co and Mn/Fe is strong.

Acknowledgments

We thank Dr. T. Kuhn for providing GTV samples and for his comments on an earlier version of the manuscript. The following colleagues are also thanked for their advice and technical assistance in the laboratory and at synchrotron facilities: S. Fakra, M. Fukukawa, J.L. Hazemann, H. Ishisako, N. Kishikawa M. Murakami, M. Nomura, O. Proux, N. Sakakibara, Y. Shibata, Y. Shimamoto, and T. Uruga. The final version of the manuscript benefited from the careful reviews by three anonymous referees. We thank the Geological Survey of Japan (GSJ), the US Geological Survey (USGS), and the Metal Mining Agency of Japan for providing samples. This research was supported by a Grant-in-Aid for scientific research from the Ministry of Education, Science, Sports, and Culture of Japan. This work has been performed with the approval of KEK (Proposal No. 2000G267), JASRI (Proposal No. 2000B0276), and the French-CRG program of the CNRS at ESRF. The ALS is supported by the Director, Office of Energy Research, Office of Basic Energy Sciences, Materials Sciences Division of the U.S. Department of Energy, under Contract No. DE-AC02-05CH11231.

Associate editor: George R. Helz

Appendix A. Supplementary data

Supplementary data associated with this article can be found, in the online version, at doi:10.1016/j.gca.2006.11.016.

References

Addy, S.K., 1979. Rare earth element patterns in manganese nodules and micronodules from northwest Atlantic. *Geochim. Cosmochim. Acta* **43**, 1105–1115.

Akagi, T., Masuda, A., 1998. A simple thermodynamic interpretation of Ce anomaly. *Geochem. J.* **32**, 301–314.

Ambe, S., Chen, S.Y., Ohkubo, Y., Kobayashi, Y., Maeda, H., Iwamoto, M., Yanokura, M., Takematsu, N., Ambe, F., 1995. "Multitracer" a new tracer technique—its principle, features, and application. *J. Radioanal. Nucl. Chem.* **195**, 297–303.

Anderson, M.A., Rubin, A.J., 1981. *Adsorption of Inorganics at Solid–Liquid Interfaces.* Ann Arbor Science Publishers, Inc.

Angove, M.J., Wells, J.D., Johnson, B.B., 1999. The influence of temperature on the adsorption of cadmium(II) and cobalt(II) on goethite. *J. Colloid Interface Sci.* **211**, 281–290.

Ankudinov, A.L., Rehr, J.J., 1997. Relativistic spin-dependent X-ray absorption theory. *Phys. Rev. B* **56**, 1712–1715.

Aplin, A.C., Cronan, D.S., 1985a. Ferromanganese oxide deposits from the Central Pacific Ocean. I. Encrustrations from the Line Islands Archipelago. *Geochim. Cosmochim. Acta* **49**, 427–436.

Aplin, A.C., Cronan, D.S., 1985b. Ferromanganese oxide deposits from the Central Pacific Ocean. II. Nodules and associated sediments. *Geochim. Cosmochim. Acta* **49**, 437–451.

Balistrieri, L.S., Murray, J.W., 1982. The adsorption of copper, lead, zinc, and cadmium on goethite from major ion seawater. *Geochim. Cosmochim. Acta* **46**, 1253–1265.

Bargar, J.R., Brown Jr., G.E., Parks, G.A., 1997a. Surface complexation of Pb(II) at oxide–water interfaces: I. XAFS and bond-valence determination of mononuclear and polynuclear Pb(II) sorption products on aluminum oxides. *Geochim. Cosmochim. Acta* **61**, 2617–2637.

Bargar, J.R., Brown Jr., G.E., Parks, G.A., 1997b. Surface complexation of Pb(II) at oxide–water interfaces: II. XAFS and bond-valence determination of mononuclear and polynuclear Pb(II) sorption products on iron oxides. *Geochim. Cosmochim. Acta* **61**, 2639–2652.

Bargar, J.R., Brown Jr., G.E., Parks, G.A., 1998. Surface complexation of Pb(II) at oxide–water interfaces: III. XAFS determination of Pb(II) and Pb(II)-chloro adsorption complexes on goethite and alumina. *Goochim. Cosmochim. Acta* **62**, 193–207.

Bau, M., 1999. Scavenging of dissolved yttrium and rare earths by precipitating iron oxyhydroxide: experimental evidence for Ce oxidation, Y–Ho fractionation, and lanthanide tetrad effect. *Goochim. Cosmochim. Acta* **63**, 67–77.

Betekhtin, A.G. 1940. South Urals manganese deposits as a raw material base for the Magnitogorsk mettallurgic plant. *Trudi Inst. Geol. Scien. Acad. Sci. USSR, Ore deposit Ser*. No. 4.

Bianconi, A., 1988. XANES spectroscopy. In: Koningsberger, D.C., Prins, R. (Eds.), *X-ray Absorption. Principles, Applications, Techniques of EXAFS, SEXAFS and XANES*. John Wiley, New York, pp. 573–662.

Brookins, D.G., 1988. *Eh–pH Diagrams for Geochemistry*. Springer-Verlag, Berlin.

Burns, R.G., 1976. The uptake of cobalt into ferromanganese nodules, soils, and synthetic manganese(IV) oxides. *Geochim. Cosmochim. Acta* **40**, 95–102.

Byrne, R.H., 2002. Inorganic speciation of dissolved elements in seawater: the influence of pH on concentration ratios. *Geochem. Trans.* **3**, 11–16.

Calvert, S.E., Piper, D.Z., 1984. Geochemistry of ferromanganese nodules from DOMES Site A, Northern Equatorial Pacific: multiple diagenetic metal sources in the deep sea. *Geochim. Cosmochim. Acta* **48**, 1913–1928.

Choi, Y.G., Kim, K.H., Chernov, V.A., Heo, J., 1999. Pb L_{III}-edge EXAFS and XANES analyses on the structural environment of lead in PbO–Ga_2O_3 glasses. *J. Non-Cryst. Solids* **246**, 128–135.

Chukhrov, F.V., Gorshkov, A.I., 1981. Iron and manganese oxide minerals in soils. *Trans. R. Soc. Edinb.* **72**, 195–200.

Cornu, S., Deschatrettes, W., Salvador-Blanes, S., Clozel, B., Hardy, M., Branchut, S., Le Forestier, L., 2005. Trace element accumulation in Mn–Fe-oxide nodules of a planosolic horizon. *Geoderma* **125**, 11–24.

Coughlin, B.R., Stone, A.T., 1995. Nonreversible adsorption of divalent metal ions (Mn^{II}, Co^{II}, Ni^{II}, Cd^{II}, and Pb^{II}) onto goethite: effects of acidification, Fe^{II} addition, and picolinic acid addition. *Environ. Sci. Technol.* **29**, 2445–2455.

Crozier, E.D., 1997. A review of the current status of XAFS spectroscopy. *Nucl. Instrum. Meth. Phys. Res. B* **133**, 134–144.

Davison, W., 1993. Iron and manganese in lakes. *Earth Sci. Rev.* **34**, 119–163.

De Baar, H.J.W., German, R.C., Elderfield, H., Van Gaans, P., 1988. Rare earth elements distributions in anoxic waters of the Cariaco Trench. *Geochim. Cosmochim. Acta* **52**, 1203–1219.

De Carlo, E.H., McMurtry, G.M., 1992. Rare-earth element geochemistry of ferromanganese crusts from the Hawaiian Archipelago, Central Pacific. *Chem. Geol.* **95**, 235–250.

Dillard, J.G., Koppelman, M.H., Crowther, D.L., Schenk, C.V., Murray, J.W., Balistrieri, L., 1981. X-ray photoelectron spectroscopic (XPS) studies on the chemical nature of metal ions adsorbed on clays and minerals. In: Tewari, P.H. (Ed.), *Adsorption From Aqueous Solutions*. Plenum Press, New York, pp. 227–240.

Dillard, J.G., Crowther, D.L., Murray, J.W., 1982. The oxidation states of cobalt and selected metals in the Pacific ferromanganese nodules. *Geochim. Cosmochim. Acta* **46**, 755–759.

Dixon, J.B., Skinner, H.C.W., 1992. Manganese minerals in surface environments. In: Skinner, H.C.W., Fitzpatrick, R.W. (Eds.), *Biomineralization Processes of Iron and Manganese. Modern and Ancient Environments*. Catena Verlag, pp. 31–50.

Drits, V.A., Sakharov, B.A., Salyn, A.L., Manceau, A., 1993. Structural model for ferrihydrite. *Clay Miner.* **28**, 185–208.

Drits, V.A., Lanson, B., Bougerol-Chaillout, C., Gorshkov, A.I., Manceau, A., 2002. Structure of heavy metal sorbed birnessite. Part 2. Results from electron diffraction. *Am. Mineral.* **87**, 1646–1661.

Dymond, J., Lyle, B., Finney, B., Piper, D.Z., Murphy, K., Conard, R., Pisias, N., 1984. Ferromanganese nodules from MANOP Sites H, S, and R—control of mineralogical and chemical composition by multiple accretionary processes. *Geochim. Cosmochim. Acta* **48**, 931–949.

Faure, G., 1998. *Principles and Applications of Geochemistry*, second ed. Princeton Hall, New Jersey, pp. 513.

Ford, R.G., Kemner, K.M., Bertsch, P.M., 1999. Influence of sorbate–sorbent interactions on the crystallization kinetics of nickel- and lead-ferrihydrite coprecipitates. *Geochim. Cosmochim. Acta* **63**, 39–48.

Gilmore, E.A., Evans, G.J., Ho, M.D., 2001. Radiochemical assessment of the readsorption and redistribution of lead in the SM&T sequential extraction procedure. *Anal. Chim. Acta* **439**, 139–151.

Glasby, G.P., 2000. Manganese: predominant role of nodules and crusts. In: Schulz, H.D., Zabe, M. (Eds.), *Marine Geochemistry*. Springer, Berlin, pp. 335–372.

Goldberg, E.D., 1961. Chemistry in the Oceans. In: Sears, M. (Ed.), *Oceanography*, vol. 67. Am. Assoc. Adv. Sci. Publ., pp. 583–597.

Goldberg, E.D., Koide, M., Schmitt, R., Smith, R., 1963. Rare-earth distributions in the marine environment. *J. Geophys. Res.* **68**, 4209–4217.

Goldberg, E.D., 1965. Minor elements in sea-water. In: Riley, J.P., Skirrow, G. (Eds.), *Chemical Oceanography*, vol. 1. Academic Press, pp. 163–196.

Halbach, P., Segl, M., Puteanus, D., Mangini, A., 1983. Co-fluxes and growth rates in ferromanganese deposits from central Pacific seamount areas. *Nature* **304**, 716–719.

Halbach, P., Friendrich, G., von Stackelberg, U., 1988. *The Manganese Nodule Belt of the Pacific Ocean*. Enke, Stuttgart.

Haley, B.A., Klinkhammer, G.P., McManus, J., 2004. Rare earth elements in pore waters of marine sediments. *Geochim. Cosmochim. Acta* **68**, 1265–1279.

Hazemann, J.L., Nayouf, K., Debergevin, F., 1995. Modelization by finite-elements of sagittal focusing. *Nucl. Instr. Meth. Phys. Res.* **B97**, 547–550.

Hem, J.D., 1978. Redox processes at surfaces of manganese oxide and their effects on aqueous metal ions. *Chem. Geol.* **21**, 199–218.

Hochella, M.F., Kasama, T., Putnis, A., Putnis, C.V., Moore, J.N., 2005a. Environmentally important, poorly crystalline Fe/Mn hydrous oxides: ferrihydrite and a possibly new vernadite-like mineral from the Clark Fork River Superfund Complex. *Am. Mineral.* **90**, 718–724.

Hochella, M.F., Kasama, T., Putnis, A., Putnis, C.V., Moore, J.N., 2005b. Direct observation of heavy metal-mineral association from the Clark Fork River Superfund Complex: implications for metal transport and bioavailability. *Geochim. Cosmochim. Acta* **69**, 1651–1663.

Hu, Z., Bertram, S., Kaindl, G., 1994. X-ray-absorption study of PrO_2 at high pressure. *Phys. Rev. B* **49**, 39–43.

Hudson-Edwards, K.A., 2000. Heavy metal-bearing Mn oxides in river channel and floodplain sediments. In: Cotter-Howells, J.D., Campbell, L.S., Valsami-Jones, E., Batchelder, M. (Eds.), *Environmental Mineralogy: Microbial Interactions, Anthropogenic Influences, Contaminated Land and Waste Management*, vol. 9. Mineralogical Society, London, pp. 207–226.

Jeon, B.-H., Dempsey, B.A., Burgos, W.D., Royer, R.A., 2003. Sorption kinetics of Fe(II), Zn(II), Co(II), Ni(II), Cd(II), and Fe(II)/Me(II) onto hematite. *Water Res.* **37**, 4135–4142.

Jo, T., Kotani, A., 1985. Theory of core photoabsorption spectra in CeO_2. *Solid State Commun.* **54**, 451–456.

Kaindl, G., Schmiester, G., Sampathkumaran, E.V., Wachter, P., 1988. Pressure-induced changes in L_{III} X-ray-absorption near-edge structure of CeO_2 and CeF_4: Relevance to 4f-electronic structure. *Phys. Rev. B* **38**, 10174–10177.

Kawabe, I., Ohta, A., Miura, N., 1999. Distribution coefficients of REE between Fe oxyhydroxide precipitates and NaCl solutions affected by REE-carbonate complexation. *Geochem. J.* **33**, 181–197.

Koschinsky, A., Halbach, P., 1995. Sequential leaching of marine ferromanganese precipitates: genetic implications. *Geochim. Cosmochim. Acta* **59**, 5113–5132.

Koschinsky, A., Hein, J.R., 2003. Uptake of elements from seawater by ferromanganese crusts: solid-phase associations and seawater speciation. *Mar. Geol.* **198**, 331–351.

Koschinsky, A., Stascheit, A., Bau, M., Halbach, P., 1997. Effects of phosphatization on the geochemical and mineralogical composition of marine ferromanganese crusts. *Geochim. Cosmochim. Acta* **61**, 4079–4094.

Kotani, A., Okada, K., Okada, M., 1987. Theory of 3d-XPS and L_3-XAS in CeF_4. *Solid State Commun.* **64**, 1479–1482.

Kuhn, T., Bau, M., Blum, N., Halbach, P., 1998. Origin of negative Ce anomalies in mixed hydrothermal-hydrogenetic Fe–Mn crusts from the Central Indian Ridge. *Earth Planet Sci. Lett.* **163**, 207–220.

Kuhn, T., Bostick, B.C., Koschinsky, A., Halbach, P., Fendorf, S., 2003. Enrichment of Mo in hydrothermal Mn precipitates: possible Mo sources, formation process and phase associations. *Chem. Geol.* **199**, 29–43.

Langmuir, D., 1997. *Aqueous Environmental Geochemistry*. Prentice-Hall, New Jersey, 350 pp.

Lanson, B., Drits, V.A., Gaillot, A.C., Silvester, E., Plançon, A., Manceau, A., 2002a. Structure of heavy metal sorbed birnessite. Part I. Results from X-ray diffraction. *Am. Mineral.* **87**, 1631–1645.

Lanson, B., Drits, V.A., Feng, Q., Manceau, A., 2002b. Crystal structure determination of synthetic Na-rich birnessite: evidence for a triclinic one-layer cell. *Am. Mineral.* **87**, 1662–1671.

Latrille, C., Elsass, F., van Oort, F., Denaix, L., 2001. Physical speciation of trace metals in Fe–Mn concretions from a rendzic lithosol developed on Sinemurian limestones (France). *Geoderma* **100**, 127–146.

Leciejewicz, J., 1961. On the crystal structure of tetragonal (red) PbO. *Acta Cryst.* **14**, 1304–1305.

Liu, F., Colombo, C., Adamo, P., He, J.Z., Violante, A., 2002. Trace elements in manganese-iron nodules from a Chinese Alfisol. *Soil Sci. Soc. Am. J.* **66**, 661–670.

Manceau, A., Llorca, S., Calas, G., 1987. Crystal chemistry of cobalt and nickel in lithiophorite and asbolane from New Caledonia. *Geochim. Cosmochim. Acta* **51**, 105–113.

Manceau, A., Charlet, L., 1992. X-ray absorption spectroscopic study of the sorption of Cr(III) at the oxide/water interface. I Molecular mechanism of Cr(III) oxidation on Mn oxides. *J. Colloid Interface Sci.* **148**, 443–458.

Manceau, A., Gorshkov, A.I., Drits, V.A., 1992a. Structural chemistry of Mn, Fe, Co, and Ni in manganese hydrous oxides: Part I. Information from XANES spectroscopy. *Am. Mineral.* **77**, 1133–1143.

Manceau, A., Charlet, L., Boisset, M.C., Didier, B., Spadini, L., 1992b. Sorption and speciation of heavy metals on Fe and Mn hydrous oxides. From microscopic to macroscopic. *Appl. Clay Sci.* **7**, 201–223.

Manceau, A., Boisset, M.C., Sarret, G., Hazemann, J.L., Mench, M., Cambier, P., Prost, R., 1996. Direct determination of lead speciation in contaminated soils by EXAFS spectroscopy. *Environ. Sci. Technol.* **30**, 1540–1552.

Manceau, A., Drits, V.A., Silverster, E., Bartoli, C., Lanson, B., 1997. Structural mechanism of Co^{2+} oxidation by the phyllomanganate buserite. *Am. Mineral.* **82**, 1150–1175.

Manceau, A., Chateigner, D., Gates, W.P., 1998. Polarized EXAFS, distance-valence least-squares modeling (DVLS) and quantitative texture analysis approaches to the structural refinement of Garfield nontronite. *Phys. Chem. Miner.* **25**, 347–365.

Manceau, A., Lanson, B., Drits, V.A., Hazemann, J.L., Gorshkov, A., Chaillout-Bougerol, C., 1999. Sorption mechanism of Zn, Cu, and Pb on birnessite by X-ray and electron diffraction, and powder and polarized EXAFS spectroscopy. EUG10, March 28-April 1, *Journal of Conference Abstracts* **4**, 666.

Manceau, A., Lanson, B., Drits, V.A., 2002a. Structure of heavy metal sorbed birnessite. Part III. Results from powder and polarized extended X-ray absorption fine structure spectroscopy. *Geochim. Cosmochim. Acta* **66**, 2639–2663.

Manceau, A., Marcus, M.A., Tamura, N., 2002b. Quantitative speciation of heavy metals in soils and sediments by synchrotron X-ray techniques. *Rev. Miner. Geochem.* **49**, 341–428.

Manceau, A., Tamura, N., Celestre, R.S., MacDowell, A.A., Geoffroy, N., Sposito, G., Padmore, H.A., 2003. Molecular-scale speciation of Zn and Ni in soil ferromanganese nodules from loess soils of the Mississippi basin. *Environ. Sci. Technol.* **37**, 75–80.

Manceau, A., Tommaseo, C., Rihs, S., Geoffroy, N., Chateigner, D., Schlegel, M., Tisserand, D., Marcus, M.A., Tamura, N., Chen, Z.S., 2005. Natural speciation of Mn, Ni and Zn at the micrometer scale in a clayey paddy soil using X-ray fluorescence, absorption, and diffraction. *Geochim. Cosmochim. Acta* **69**, 4007–4034.

Manceau, A., Lanson, M., Geoffroy, N., 2007. Natural speciation of Ni, Zn, Ba and As in ferromanganese coatings on quartz using X-ray fluorescence, absorption, and diffraction. *Geochim. Cosmochim. Acta,* **71**, 95–128.

Mannheim, F.T., Lane-Bostwick, C.M., 1988. Cobalt in ferromanganese crusts as a monitor of hydrothermal discharge on the Pacific seafloor. *Nature* **335**, 59–62.

Marcus, M.A., Manceau, A., Kersten, M., 2004a. Mn, Fe, Zn and As speciation in a fast-growing ferromanganese marine nodule. *Geochim. Cosmochim. Acta* **68**, 3125–3136.

Marcus, M., MacDowell, A.A., Celestre, R., Manceau, A., Miller, T., Padmore, H.A., Sublett, R.E., 2004b. Beamline 10.3.2 at ALS: a hard X-ray microprobe for environmental and materials sciences. *J. Synchrotron Radiat.* **11**, 239–247.

Martin, J.H., Gordon, R.M., Fitzwater, S., Broenkow, W.W., 1989. VERTEX: phytoplankton/iron studies in the Gulf of Alaska. *Deep-Sea Res.* **36**, 649–680.

Matocha, C.J., Elzinga, E.J., Sparks, D.L., 2001. Reactivity of Pb(II) at the Mn(III,IV) (oxyhydr)oxide–water interface. *Environ. Sci. Technol.* **35**, 2967–2972.

McKenzie, R.M., 1989. Manganese oxides and hydroxides. In: Dixon, J.B., Weed, S.B. (Eds.), *Minerals in Soil Environments*, *Soil Science Society of America book series*, vol. 1. Soil Science Society of America, Madison, pp. 439–465.

McLennan, S.M., 1989. Rare earth elements in sedimentary rocks: influence of provenance and sedimentary processes. *Rev. Miner.* **21**, 169–200.

Moffett, J.W., Ho, J., 1996. Oxidation of cobalt and manganese in seawater via a common microbially catalyzed pathway. *Geochim. Cosmochim. Acta* **60**, 3415–3424.

Moorby, S.A., Cronan, D.S., 1981. The distribution of elements between co-existing phases in some marine ferromanganese-oxide deposits. *Geochim. Cosmochim. Acta* **45**, 1855–1877.

Morin, G., Ostergren, J.D., Juillot, F., Ildefonse, P., Calas, G., Brown, G.E.Jr., 1999. XAFS determination of the chemical form of lead in smelter-contaminated soils and mine tailings: importance of adsorption processes. *Am. Mineral.* **84**, 420–434.

Morin, G., Juillot, F., Ildefonse, P., Calas, G., Samama, J.C., Chevallier, P., Brown, G.E. Jr., 2001. Mineralogy of lead in a soil developed on a Pb-mineralized sandstone (Largentière, France). *Am. Mineral.* **86**, 92–104.

Murray, J.W., 1974. The surface chemistry of hydrous manganese dioxide. *J. Colloid Interface Sci.* **46**, 357–371.

Murray, J.W., Dillard, J.G., 1979. The oxidation of cobalt(II) adsorbed on manganese dioxide. *Geochim. Cosmochim. Acta* **43**, 781–787.

Nishimura, M., 1983. *Marien Chemistry*. Sangyo Tosho, Tokyo, pp. 82–83 (in Japanese).

Nomura, M., Koyama, A., 1996. Design and performance of a new XAFS beamline at the photon factory; BL-12C. *KEK Report* **95–15**.

Nomura, M., 1998. Dead-time correction of a multi-element SSD for fluorescent XAFS. *J. Synchrotron Radiat.* **5**, 851–853.

Ohta, A., Ishii, S., Sakakibara, M., Mizxuno, A., Kawabe, I., 1999. Systematic correlation of the Ce anomaly with the Co/(Ni + Cu) ratio and Y fractionation from Ho in distinct types of Pacific deep-sea nodules. *Geochem. J.* **33**, 399–417.

Piepgras, D.J., Jacobsen, S.B., 1992. The behavior of rare earth elements in seawater: precise determination of variations in the North Pacific water column. *Geochim. Cosmochim. Acta* **56**, 1851–1862.

Piper, D.Z., 1974. Rare earth elements in ferromanganese nodules and other marine phases. *Geochim. Cosmochim. Acta* **38**, 1007–1022.

Pozas, R., Rojas, T.C., Ocana, M., Serna, C.J., 2004. The nature of Co in synthetic Co-substituted goethites. *Clay Clay Miner.* **52**, 760–766.

Proux, O., Nassif, V., Prat, A., Ulrich, O., Lahera, E., Biquard, X., Menthonnex, J.J., Hazemann, J.L., 2006. Feedback system of a liquid-nitrogen-cooled double-crystal monochromator: design and performances. *J. Synchrotron Rad.* **13**, 59–68.

Rao, K.J., Wong, J., 1984. A XANES investigation of the bonding of divalent lead in solids. *J. Chem. Phys.* **81**, 4832–4843.

Rendell, P.S., Batley, G.E., Cameron, A.J., 1980. Adsorption as a control of metal concentrations in sediment extracts. *Environ. Sci. Tehnol.* **14**, 314–318.

Ressler, J., 1998. WinXAS: a program for x-ray absorption spectroscopy data analysis under MS-Windows. *J. Synchrotron Rad.* **5**, 118–122.

Rouse, R.C., 1971. The crystal structure of quenselite. *Zeit. Krist.* **134**, 321–332.

Schaule, B.K., Patterson, C.C., 1981. Lead concentrations in the northeast Pacific: evidence for global anthropogenic perturbations. *Earth Planet. Sci. Lett.* **54**, 97–116.

Scheinost, A.C., Abend, S., Pandya, K.I., Sparks, D.L., 2001. Kinetic controls on Cu and Pb sorption by ferrihydrite. *Environ. Sci. Technol.* **35**, 1090–1096.

Schlegel, M.L., Manceau, A., Charlet, L., Chateigner, D., Hazemann, J.L., 2001. Sorption of metal ions on clay minerals. III. Nucleation and epitaxial growth of Zn phyllosilicate on the edges of hectorite. *Geochim. Cosmochim. Acta* **65**, 4155–4170.

Schwertmann, U., Cornell, R.M., 2000. *Iron Oxides in the Laboratory*. Wiley-VCH, Weinheim, pp. 67–112.

Sholkovitz, E.R., 1989. Artifacts associated with the chemical leaching of sediments for rare-earth elements. *Chem. Geol.* **77**, 47–51.

Silvester, E., Manceau, A., Drits, V.A., 1997. The structure of synthetic monoclinic Na-rich birnessite and hexagonal birnessite. Part 2. Results from chemical studies and EXAFS spectroscopy. *Am. Mineral.* **82**, 962–978.

Smedley, P.L., Kinniburgh, D.G., 2002. A review of the source, behaviour and distribution of arsenic in natural waters. *Appl. Geochem.* **17**, 517–568.

Soldatov, A.V., Ivanchenko, T.S., Longa, S.D., Kotani, A., Iwamoto, Y., Bianconi, A., 1994. Crystal-structure effects in the Ce L_3-edge X-ray absorption spectrum of CeO_2: multiple-scattering resonances and many-body final states. *Phys. Rev. B* **50**, 5074–5080.

Sorem, R.K., Fewkes, R.H., 1977. Internal characteristics. In: Glasby, G.P. (Ed.), *Marine Manganese Deposits*. Elsevier, Amsterdam, pp. 147–183.

Spadini, L., Manceau, A., Schindler, P.W., Charlet, L., 1994. Structure and stability of Cd^{2+} surface complexes on ferric oxides. I. Results from EXAFS spectroscopy. *J. Colloid Interface Sci.* **168**, 73–86.

Spadini, L., Schindler, P.W., Charlet, L., Manceau, A., Ragnarsdottir, K.V., 2003. Hydrous ferric oxide: evaluation of Cd–HFO surface complexation models combining Cd_K EXAFS data, potentiometric titration results, and surface site structures identified from mineralogical knowledge. *J. Colloid Interface Sci.* **266**, 1–18.

Stumm, W., 1993. *Chemistry of the Solid–Water Interface*. John Wiley & Sons.

Sumaoka, J., Igawa, T., Furuki, K., Komiyama, M., 2000. Homogeneous Ce(IV) complexes for efficient hydrolysis of plasmid DNA. *Chem. Lett.* **29**, 56–57.

Szytula, A., Burewicz, A., Dimitrijevic, Z., Krasnicki, S., Rzany, H., Todorovic, J., Wanic, A., Wolski, W., 1968. Neutron diffraction studies of α-FeOOH. *Phys. Stat. Sol.* **26**, 429–434.

Takahashi, Y., Minai, Y., Ambe, H., Makide, Y., Ambe, F., Tominaga, T., 1997. Simultaneous determination of stability constants of humate complexes with various metal ions using multitracer technique. *Sci. Total Environ.* **198**, 61–71.

Takahashi, Y., Minai, Y., Ambe, H., Makide, Y., Ambe, F., 1999. Comparison of adsorption behavior of multiple inorganic

ions on kaolinite and silica in the presence of humic acid using the multitracer technique. *Geochim. Cosmochim. Acta* **63**, 815–836.

Takahashi, Y., Shimizu, H., Usui, A., Kagi, H., Nomura, M., 2000. Direct observation of tetravalent cerium in ferromanganese nodules and crusts by X-ray absorption near-edge structure (XANES). *Geochim. Cosmochim. Acta* **64**, 2929–2935.

Takahashi, Y., Sakami, H., Nomura, M., 2002a. Determination of the oxidation state of cerium in rocks by Ce L_{III}-edge X-ray absorption near-edge structure. *Anal. Chim. Acta* **468**, 345–354.

Takahashi, Y., Usui, A., Okumura, K., Uruga, T., Nomura, M., Murakami, M., Shimizu, H., 2002b. Application of XANES for the determination of oxidation states of Co and Pb in natural ferromanganese nodules. *Chem. Lett.* **31**, 366–367.

Takematsu, N., Sato, Y., Okabe, S., 1989. Factors controlling the chemical composition of marine manganese nodules and crusts: a review and synthesis. *Mar. Chem.* **26**, 41–56.

Takematsu, N., 1998. *Manganese nodule*. Koseisha Kouseikaku, Tokyo (in Japanese).

Teo, B.K., 1986. *EXAFS: Basic Principles and Data Analysis*. Springer-Verlag.

Terashima, S., Usui, A., Imai, N., 1995. 2 new GSJ geochemical reference samples—syenite JSy-1 and manganese-nodule JMn-1. *Geostandards Newslett.* **19**, 221–229.

Toner, B., Manceau, A., Webb, S.M., Sposito, G., 2006. Zinc sorption to biogenic hexagonal-birnessite particles within a hydrated bacterial biofilm. *Geochim. Cosmochim. Acta* **70**, 27–43.

Trivedi, P., Dyer, J.A., Sparks, D.L., 2003. Lead sorption onto ferrihydrite. 1. A macroscopic and spectroscopic assessment. *Environ. Sci. Technol.* **37**, 908–914.

Uruga, T., Tanida, H., Yoneda, Y., Takeshita, K., Emura, S., Takahash, M., Harada, M., Nishihata, Y., Kubozono, Y., Tanaka, T., Yamamoto, T., Maeda, H., Kamishima, O., Takabayashi, Y., Nakata, Y., Kimura, H., Goto, S., Ishikawa, T., 1999. The XAFS beamline BL01B1 at SPring-8. *J. Synchrotron Rad.* **6**, 143–145.

Usui, A., Bau, M., Yamazaki, T., 1997. Manganese microchimneys buried in the Central Pacific pelagic sediments: evidence of intraplate water circulation? *Mar. Geol.* **141**, 269–285.

Villalobos, M., Toner, B., Bargar, J., Sposito, G., 2003. Characterization of the manganese oxide produced by *Pseudomonas putida* strain MnB1. *Geochim. Cosmochim. Acta* **67**, 2649–2662.

Villalobos, M., Bargar, J., Sposito, G., 2005. Mechanisms of Pb(II) sorption on a biogenic manganese oxide. *Environ. Sci. Technol.* **39**, 569–576.

Villalobos, M., Lanson, B., Manceau, A., Toner, B., Sposito, G., 2006. Structural model for the biogenic Mn oxide produced by *Pseudomonas putida*. *Am. Mineral.* **91**, 489–502.

Vodyanitskii, Y.N., Sivtsov, A.V., 2004. Formation of ferrihydrite, ferroxyhyte, and vernadite in soil. *Eurasian Soil Sci.* **37**, 863–875.

Wehrli, B., 1990. Redox reactions of metal ions at mineral surfaces. In: Stumm, W. (Ed.), *Aquatic Chemical Kinetics*. Wiley, New York, pp. 311–336.

Wen, X., De Carlo, E.H., Li, Y.H., 1997. Interelement relationships in ferromanganese crusts from the central Pacific ocean: their implications for crust genesis. *Mar. Geol.* **136**, 277–297.